A prefrontal motor circuit initiates persistent movement

Authors: Yihan Wang[1,2] and Qian-Quan Sun[1,2,3*]

Affiliations:

[1]Graduate Neuroscience Program, University of Wyoming, Laramie, WY82071, USA

[2]Department of Zoology and Physiology, University of Wyoming, Laramie, WY82071, USA

[3]Wyoming Sensory Biology Center of Biomedical Research Excellence, University of Wyoming, Laramie, WY82071, USA

*Correspondence: Dr. Qian-Quan Sun, neuron@uwyo.edu, Phone (307) 766 5602

Abstract

Persistence ensures continuity in a course of action. It is crucial to human success and animal survival. However, how the brain applies persistence to movements is unknown. Here we demonstrate that persistence arises during the initial phase of movement and is maintained until terminal signaling. Using single-unit extracellular recordings in awake mice, we found that neural encoding of persistent movement phases is independent of the valuation (i.e., valence) of the external stimuli. Next, using opto-tagging, we identified a group of dorsal medial prefrontal cortex (dmPFC) motor cortex projecting (MP) neurons, which encodes the initial phase of a persistent movement rather than valence. Inactivation of dmPFC MP neurons impairs the initiation of persistence and reduces neuronal activity in the insular and motor cortex. Finally, a computational model suggests that a successive sensory stimulus acts as a triggering signal for the initiation of persistent movements. These results reveal a neural mechanism that switches the brain state from neutral to persistent during movement.

Introduction

Persistence is a fundamental property that can help humans succeed in many areas, such as athletic and social competition [1, 2]. It has a long-lasting effect on the maintenance of motivation [3]. It also contributes to the animal's survival, such as dominating in social hierarchy and escaping from predators [4]. It can drive actions successively from seconds to minutes and even outlast the eliciting stimulus. Socially dominant animals exhibit effortful behaviors toward their rivals [5]. Repeated visual threat stimuli lead a persistent state in *Drosophila* [6]. Although persistence is influential in both humans and animals, there are few studies on how the brain applies it to movements. Moreover, the psychological definition of persistence is not appropriate to solve certain behavioral problems, including how long it should last and how to quantify its continuity, as it can vary from behavior to behavior. To examine persistence, we focus on a motivated movement [7] that can persist for a certain period of time and stabilize at a range of high frequency. This type of motivated movement is triggered by internal states from deep brain regions and is regulated by cortex neurons [7, 8, 9]. It is also accompanied with extensive valence coding in the brain [10, 11, 12, 13]. Here, we attempt to identify the neural coding in the different phases of motivated, persistent movement and to test whether it is the same with the coding of valence.

Quantification of persistent movements

First, we defined a persistent movement as the continuous repetition of a single movement (e.g., a cycle of tongue or limb movements) and the maintenance of that continuity for at least 5 seconds. To impose a persistent movement on mice, they were deprived of water for 16 to 36 hours until their body weight decreased by about 22% (Subject details, **Methods**). The mice were then head-fixed to a custom made set-up and trained to lick various types of liquid after delivery onset (DO) (**Fig. 1a**, **Supplementary Fig. 1b**, and Behavioral details, **Methods**), but received no other artificial stimuli. Licking signals, facial and locomotor activities were measured. After training, we observed that the mice showed licking movements sustained for approximately 15-30 seconds during water delivery (**Supplementary Fig. 1c-f**). Consistent with the standard pattern of affective dynamics performed previously [14], licking frequency was maximized during the initial phase (**Supplementary Fig. 1c-f**, right column, peaks of licking frequency are indicated by black arrows) and then stabilized at 6 to 7 Hz until the end of delivery (**Supplementary Fig. 1d, e**) or when the liquid was switched to quinine (5mM, **Supplementary Fig. 1c, f**). Higher hedonic stimuli, 20% sucrose, did not increase this frequency (**Supplementary Fig. 1e, f**). As an aversive stimulus, quinine administration was more likely than the interruption of water or sucrose administration to cause termination of persistent licking ($p<0.05$ with respect to termination bias, **Supplementary Fig. 1i**). In addition, we found no significant difference between male and female mice in the initiation and termination of persistent licking movement (**Supplementary Fig. 1r, s**). Therefore, quinine was used to terminate the persistent licking movement and to evaluate negative valence; by contrast, water or sucrose was used to trigger licking movement and to evaluate positive valence.

Next, we determined the temporal window for the study of valence and movement phases. For valence, the assessment of whether water or quinine is hedonic or aversive should be based on the single contact (approximately 180ms around the licking onset (LO), **Supplementary Fig. 1c-f**) to them. For movement phase, we divided it into an initial and a terminal phase. To our observation, the maximum licking frequency was confined within the initial phase and a sharp decrease of licking frequency was in the terminal phase (**Supplementary Fig. 1c-f**), so we suspected that there was additional neural coding to increase and decrease licking frequency besides the coding of licking command. Based on the period of peak licking frequency (approximately 3s, as indicated by the arrow, **Supplementary Fig. 1c**) in the initial phase and the sharp drop of licking frequency (approximately 3s from 6-7 Hz to less than 1 Hz, as indicated by the arrow, **Supplementary Fig. 1c**) in the terminal phase, we designed a time window of 5-second long (including 2s baseline before the licking onset) as a temporal window for data analysis. Together, we considered the neuronal firings of the valence and movement phases were confined within a small (S, LO-100ms to LO+80ms) and a large (L, 1st LO-2s to 1st LO+3s) scale window, respectively (**Fig. 1c**).

Dissociable neural coding of movement phases and valence

To characterize the single-units that statistically represent valence and movement phases, we used *in vivo* silicon probe to collect neuronal activity data from all three brain regions, including the insular cortex (IC), which is known to encode valence in the gustatory system [11, 15], the primary motor cortex (M1), which represents the motor commands of voluntary movement [16], and the dorsal medial prefrontal cortex (dmPFC), which has been shown to connect these two brain regions [17]. The single-units that were generated from the neural activity data were then classified into different groups of neural representations according to the extent to which they can discriminate liquid types (for valence) or movement phases (**Methods**).

We then asked whether the neuronal coding of movement phases and valence are associable or not by examining the proportion of neural representations of valence and movement phases in three brain regions (IC, M1, and dmPFC). As population, we found that 27% of single-units represented movement phases (initial or terminal phase, ≥65% in movement phase correlation) but showed weak or no taste tuning (**Fig. 1d-f**). 14% of single-units represented valence (positive or negative valence (PV or NV), z>1.64 in taste correlation) but exhibited poor specification on movement phases (**Fig. 1d-f**). By contrast, only small fraction (8%) of single units displayed the preference to both valence and movement phases (**Fig. 1e, f**), though this number varied trivially from region to region (**Supplementary Fig. 4**).

To test whether the neural networks representing movement phases and valence interact with each other, we examined the connectivity between the neurons solely tuned to initial phase and PV using Total Spiking Probability Edges (TSPE) [18] and compared it with shuffled connectivity. Our results showed that there is no overall excitatory impact from the initial phase to PV or from PV to initial phase tuned neurons (mean of real TSPE < 99 percentile of shuffled TSPE, **Supplementary Fig. 5d**). Note that connectivity between the terminal phase and NV tuned neurons was not available because their spike data were unable to construct a cross-correlation in a 50ms-time window, suggesting that the coding of terminal phase and NV are not connected. Together, these results suggest that the movement phases and valence are encoded separately.

Coding of the initial phase in dmPFC MP neurons

Next, we investigated the neural basis representing the initial phase of persistent movement. We first compared the fraction of clustered neural representations in the IC, M1, and dmPFC. Second, we examined decoding performance in these brain regions by training a linear discriminant decoder on firing rate data. Using cell-specific recordings enabled by the opto-tagging approach [19] (**Fig. 2a-c**), we found that motor cortex projecting (MP) neurons [17] in the dmPFC exhibited the best representation of the initial phase among the three mapped brain regions (**Fig. 2, Supplementary Fig. 4, 6,** and **7**). Specifically, the neuronal clustering results showed that 32% of dmPFC MP neurons exhibited a degree (≥65% shuffled activity at initial phase & ≤35% shuffled activity at terminal phase) of initial phase representation (**Fig. 2h**), whereas only 3% of them exhibited a degree (≥65% shuffled activity at terminal phase & ≤35% shuffled activity at initial phase) of terminal phase representation (**Fig. 2h**). No more than 20% of dmPFC MP neurons showed a degree (z>1.64 in valence correlations compared to shuffled activity) of valence representation (PV+NV, **Fig. 2e**). The decoding performance results showed that dmPFC MP neurons had a low ability to discriminate positive and negative valence (p<0.0001 lower than shuffled cumulative decoding accuracy, **Fig. 2k left**), while had a high representation of movement phases (p<0.0001 higher than IC and shuffled cumulative decoding accuracy, **Fig. 2k right**). To confirm the discriminability of dmPFC MP neuron between valence and movement phases, we first embedded neuronal population activity in the S- and L-window of dmPFC MP neurons into trajectories using principal component analysis (PCA) and then measured the mean Euclidean distances in all PC dimensions. The results showed that the discrimination of neural activity was significant higher in the L-window than it in the S-window (p<0.05, **Fig. 2j**), indicating that dmPFC MP neurons discriminate better between movement phases than between valence values.

Bodily arousal is usually accompanied by valence changes [4]. It is, therefore, necessary to investigate whether or not dmPFC MP neuron also encode bodily arousal. In rodents, facial activity can reflect

bodily arousal [20]. In the persistent licking task, the facial activity showed a reliable increase immediately after water DO ($p<0.05$ compared to baseline in all sessions, **Supplementary Fig. 1k-n**). Thus, we used facial activity to assess bodily arousal in the initial phase. To investigate whether the firing changes of dmPFC MP neuron in the initial phase were due to bodily arousal, we trained a Hammerstein-Wiener model and tested its prediction accuracy using facial activity data. Although some dmPFC neurons exhibited a degree of facial activity representation in the initial phase ($p<0.05$ initial phase (median=-4.5671; 21/194 neurons with accuracy>30%) vs terminal phase (median=-36.9341; no neuron with accuracy>30%), **Supplementary Fig. 8d2**), all dmPFC MP neurons showed poor prediction performance at both initial (median=-14.5639; no neuron with accuracy>30%) and terminal phase (median=-27.4588; no neuron with accuracy>30%) on facial activity and no significant difference between these two phases ($p>0.05$, **Fig. 2l, m**). These results excluded the possible coding of bodily arousal in dmPFC MP neurons.

Effects of dmPFC MP neuron silencing on persistent movement

To test the role of dmPFC MP neuron on persistent licking movement in different phases, we examined the initiation and termination bias, as well as licking frequency (**Methods**). dmPFC MP neurons were optogenetically manipulated by expressing stGtACR2 [21] and shining laser during the different phases of the persistent licking task (**Fig. 3a**). Our results showed that optogenetic silencing of dmPFC MP neurons impaired the initiation of licking ($p<0.001$ compared to the sham trials, **Fig. 3b, c**), but had no effect on the termination of lick ($p>0.05$ compared to the sham trials, **Fig. 3d, e**) or the licking frequency in the middle phase (**Supplementary Fig. 10b2**) in thirsty mice, suggesting that dmPFC MP neurons are not involved in motor control. The similarity of thirst level was confirmed by comparing body weight loss in sham and laser trials (**Supplementary Fig. 10b4**, **c3**, and **d3**). To further confirm the function of dmPFC MP neuron in initiating persistent licking movement, dmPFC MP neurons, expressing hm4D(Gi), were chemogenetically silenced by administrating with CNO in mice and the licking chances were tested during the persistent licking task. As expected, thirsty mice with chemogenetically silenced dmPFC MP neuron had lower chance of drinking water ($p<0.05$ compared to the saline trials, **Supplementary Fig. 9c**). To investigate whether the dampened licking initiation was due to a decrease in bodily arousal, we tested facial and locomotor activity with or without optogenetic silencing. The mice in the sham and laser trials displayed the similar levels of facial and locomotor activity in all initial, middle, and terminal phase (**Fig. 3g** and **Supplementary Fig. 10b-d**), suggesting that the attenuated licking initiation was not due to the decrease of bodily arousal.

We next asked whether the effect of dmPFC MP neuron silencing was specific to the initiation of persistent licking or also general to other types of initiation of persistent behavior. We took advantage that mice showed a phase of persistent running after a mild electric shock (**Supplementary Fig. 9h**). To test whether inactivation of dmPFC MP neurons also affected this behavior, we examined body activity after a 1s electrical tail shock. Indeed, chemogenetic silencing of dmPFC MP neurons suppressed escaping behavior (**Supplementary Fig. 9h, i**), suggesting that dmPFC MP neurons are generally involved in the initiation of persistent movements. This result is consistent with previously reported general population of dmPFC neurons, silencing of which has been shown to delay the initiation of avoidance movements [9]. Together with the evidence that dmPFC MP neurons are required for the persistent licking movement, this also supports the theory of mixed selectivity in the prefrontal cortex [22].

Next, we hypothesized that the increase in the brain state of positive valence and tongue movement in the initial phase was due to the coding of movement phases. IC is thought to encode taste valence [11, 15] (38/42 in w-q vs 11/42 in w-s vs 33/42 in w-w with mean decoding accuracy higher than chance, **Supplementary Fig. 6a**), whereas M1 was involved in voluntary control of tongue movement during licking [23, 24] (12% neurons with z>1.64 in lick correlations compared with shuffled activity, **Supplementary Fig. 4b1**). Therefore, the activities in IC and M1 should be affected by the optogenetic silencing of dmPFC MP neurons. To test this hypothesis, we measured the neural activity in these two brain regions with or without shining laser on dmPFC. As expected, the neuronal activities of M1 and IC were decreased ($p<0.05$) after dmPFC MP neurons were optogenetically silenced (**Fig. 4f, g**). We further confirmed this initial phase specificity by excluding the effect of silencing of dmPFC MP neuron on valence at middle phase (no significant difference of sucrose-licking frequency between sham and laser trials, **Supplementary Fig. 10a**). Overall, our results suggest that the dmPFC MP neuron is required to initiate continuous licking, and further promoting taste valence during the initial phase, but loses its necessity upon the persistent movement already initiated.

A MP network-based computational model

Finally, we asked what causes the MP network to initiate a persistent movement. To answer this question, we built a neural network-based model (**Fig. 5a**) and examined how the output of licking performance changes in response to different types of inputs. The design of this model was mainly based on two criteria: (1) the inter-spike interval of a single neuron in the model is matched to the MP neuron in mPFC (**Supplementary Fig. 11a**); (2) the neuronal population of modeled network performs rotational dynamics [25] because we assumed that tongue movement follows a rhythmic pattern (**Supplementary Fig. 11b, c**). To verify if the output of this model matched the performance of thirsty mice in the actual experiment, we manipulated the firing rate of the simulated network by inserting the inputs with different amplitudes and examined the output licking frequency and initiation bias. We found no linear relationship between the mean neuronal firing rate and above two parameters (**Supplementary Fig. 11d**, red), which is consistent with the experimental observations (**Supplementary Fig. 11d**, black). To further ensure the feasibility of the MP network-based model, we simulated the optogenetic silencing of dmPFC MP neurons through decreasing the number of all neurons in the modeled network. Consistent with the experimental data, the network with reduced neural population inhibited the initiation of persistent lick (**Fig. 5b**). We then examined the effect of temporally continuous input on the output of the network. We found that even a single short-term interruption (200ms) disrupted the initiation of continuous lick (average 57% decrease on initiation bias, **Fig. 5c**). The percentage of bias with two interruptions decreased to 5.7±0.08% (compared with 21±1.17% with no interruption, **Fig. 5c**). This temporally continuous input of the model suggests that the triggering signal for the MP network should be intact, continuous sensory stimulation. For the persistent licking task, we suspected this sensory stimulation may come from the continuous sensation of the liquid delivery.

Summary and Discussion

Our study identified a neural circuit, responsible for initiating persistent movements. After receiving a sensory signal, dmPFC MP neurons can send the command signals to the primary motor cortex and striatum, which in turn initiates the downstream machineries for a persistent movement (**Fig. 6**). Our results excluded the possibility of the neural coding of valence, bodily arousal, and motor command by

202 dmPFC MP neurons. Our findings suggest that the engagement in persistent movement is not based
203 solely on a snap judgment of the current situation.

204 **Summary of neural principles.** Based on the membrane properties and network connectivity of MP
205 neurons, we summarized two neural principles that govern the initiation of persistent movement. First,
206 the circuits should consist of slow spiking neurons. mPFC layer V MP neurons are the main functional
207 units linking deep brain regions and motor cortex, and they fire more slowly than the pyramidal neurons
208 of layer II [17, 26]. In line with the observation of maximal licking frequency (about 8 Hz) during the initial
209 phase (**Supplementary Fig. 1c-f**), the firing rate of neurons modulating the tongue should not exceed
210 this value. Second, the circuit should be constructed with monotonic outputs and divergent inputs.
211 Within the mPFC, the projection of the MP network is relatively sparse, projecting only to the
212 contralateral dmPFC and motor regions, whereas the inputs to the MP network are originated from
213 different deep brain regions [17]. This connection configuration may help to ensure that the MP network
214 not only simultaneously receive the signals from the neurons that tuned multiple aspects of sensory
215 cues, but also regulate downstream motor output independent of other neural networks.

216 **Formation of a generalized command.** Although we have uncovered a neural basis for encoding the
217 initial phase of persistent movements, it is unclear how the generalized sensory command is formed or
218 how a specific movement is executed under a persistent pattern: First, how are the valuable aspects of
219 sensory cues recognized? This unsupervised learning process requires a generalizing neural network [27]
220 that extracts only a few optimal aspects of stimulus while maintaining specificity. The question is why
221 some of the aspects are optimal but others are not. We suspect that these optimized aspects are the
222 ones that are most similar or closest in time to the reward or punishment itself, as they can efficiently
223 and directly link to a specific behavioral pattern. Second, how can the sensory cue be associated with a
224 particular movement pattern? Based on the reciprocal link between mPFC and motor cortex [17], we
225 reason that a feedback loop between the generalization network and motor regions may be required.
226 Meanwhile, a valence input may be also necessary to construct the association and sensitize the
227 response to sensory cue.

228 **Explanation of the dynamics of valence coding.** To explain the gradually fading firings (**Supplementary**
229 **Fig. 4d, e**) of PV neural representations during water licks, we postulate two possibilities: (1)
230 Transformation of neural representations. Some neurons may initially encode PV but abolish this
231 encoding property in subsequent phases. Other neurons may not encode PV in the initial phase but
232 adopt this encoding later. This possibility can explain the persistent valence encoding in the IC
233 (**Supplementary Fig. 6a3**); (2) Valence decreases. Since the thirsty mice may become satiated as the lick
234 progresses, the value of water to the mice will decrease accordingly. Similarly, the gradually increasing
235 activity of the neural representations of NV (**Supplementary Fig. 4d, e**) could also be caused by the
236 transformation of their encoding properties or by an increasing negative valuation of water.

237 **The function of MP neuron in the IC-MP-motor circuit.** Based on the structure of the circuit, the MP
238 neuron acts as a node connecting IC and motor region [17]. Since IC encodes valence, it is possible that the
239 MP neuron integrates valence signal and sends it to motor region. However, our result showed that MP
240 neuron does not encode valence (**Fig. 2k**). Because some of the neurons in IC also encode movement
241 phases (**Fig. 2k** and **Supplementary Fig. 4a**), we speculate the function of this circuit is to transmit
242 movement phase signals, instead of valence, during persistent movement control.

243 **Relationships to persistent spiking activity.** Persistent spiking activity in prefrontal cortex has been
244 observed in both rodents and humans during the maintenance of working memory [28, 29]. However, only a
245 few neurons in the prefrontal cortex showed persistent activity (small fraction of neural representations
246 of lick, **Supplementary Fig. 4c**, and gradually decreasing firing of neural representations of PV and initial
247 phase, **Supplementary Fig. 4d, e**) during persistent licking. Rather than maintain the neural activity,
248 dmPFC MP neurons are responsible for triggering such activity in the motor cortex. Because this
249 triggering process also requires a successive, short-term (about 5s) external stimulus, we summarize the
250 function of the dmPFC MP network as converting a relatively short-term, external, persistent input into
251 a relatively long-term, internal, persistent activity.

252

253 **METHODS**

254 **Subject details**

255 All experimental procedures were approved by the Institutional Animal Care and Use Committee
256 (IACUC) and the Biosafety Committee of the University of Wyoming. 14 male and 6 female
257 immunocompetent mice of specified age (indicated in **Surgeries** and **Behavioral details**) were used for
258 various experimental purposes. All mice were bred on a C57/BL6J background. Mice older than 30 days
259 were housed with same-sex littermates or alone in a vivarium at 21-23 ^{o}C and a 12-h light/dark cycle.
260 Mice implanted with an electrode or head bar were housed alone. For chemo-genetic experiments, 2
261 male and 2 female mice received AAV injection and head bar implant. For optogenetic experiments, 6
262 male mice and 2 female mice received AAV injection, an opto-electrode, and head bar implantation. 3
263 male mice and 1 female mouse were implanted with electrodes and head bar. 1 male mouse and 1
264 female mouse were implanted with optical fibers and electrodes. Optical fibers were implanted in 2
265 male mice. For all behavioral experiments, mice were deprived of water for 16-36 hours before the
266 experimental day until they reached 75-80% of their free-feeding body weight. After each behavioral
267 experiment, mice were returned to their home cage where they had unlimited access to water for at
268 least five days until the next behavioral test day.

269 **Surgeries**

270 The preparatory procedures are similar for both implantation and injection. Mice were anesthetized
271 using oxygenated (2 LPM for induction and 0.4 LPM for maintenance) 2% isoflurane (v/v). Mice heads
272 were fixed to the stereotactic device (NARISHIGE SG -4N) and maintained at 37 ^{o}C with a heating pad
273 (K&H No. 1060). Seventy percent isopropyl alcohol and iodine were placed on the incision site. The skull
274 was exposed by cutting the skin and removing the dura and connective tissue. The coordinates used for
275 positioning the injection and implantation sites were relative to Bregma (antero-posterior A-P, medio-
276 lateral M-L, dorsal-ventral D-V) in mm. After the surgeries, the mice were administered intraperitoneal
277 ibuprofen (50 mg kg^{-1}), and they were kept at 37°C for 30-60 minutes before returning to the home
278 cage.

279 For viral injection, P14-30 mice were used. A small craniotomy (approximately 0.2 mm in diameter) was
280 made over the injection site. Glass filaments (Drummond Scientific Co.) with a tip diameter of
281 approximately 5 µm were filled with 2 µL of virus solution. By pressure injection with a custom-made
282 device driven by a single-axis hydraulic manipulator (NARISHIGE mmo-220A), the viral solution

283 (undiluted, 100 nL at each injection site) was delivered to the desired regions at a rate of 30-50 nL min^{-1}.
284 Opto-labeled dmPFC MP neurons were labeled with pAAV- CAG -hChR2-mcherry (Addgene_28017-
285 AAVrg) injected into motor cortex (A-P -0.6, M-L 1.0, D-V 0.2 0.5 0.8). For chemogenetic inhibition,
286 pAAV-Ef1a-mCherry- IRES -Cre (Addgene_55632-AAVrg) was injected into bilateral motor cortex (A-P -
287 0.6, M-L ±1.0, D-V 0.2 0.5 0.8), followed by injection of pAAV-hsyn-DIO-hm4D(Gi) (Addgene_44362-
288 AAV5) into the bilateral dmPFC (A-P 1.35, M-L ±0.2, D-V 0.2 0.5 0.8 at an angle of 30° to the upright
289 position). For optogenetic silencing, pAAV-CKIIa-stGtACR2-FusionRed (Addgene_105669-AAVrg) was
290 injected into the bilateral motor cortex (A-P -0.6, M-L ±1.0, D-V 0.2 0.5 0.8). Mice were returned to the
291 home cage until at least three weeks before implantation.

292 For implantation, silicon probes (A4x8-Edge-2mm-100-200-177-CM32 or A1x32-Edge-5mm-25-177-
293 CM32, NeuroNexus) or 32-tetrode bundles (Bio-Signal technologies) were implanted followed by optic
294 fibers and head bar. To build opto-electrode, optic fibers (MFC_200/245-0.37_2.0mm_MF1.25_FLT)
295 were fixed around 0.5 mm above the electrodes using crazy glue and dental cement (Lang Dental). In
296 opto-inhibition experiments, two optic fibers (MFC_600/710-0.37_1.0mm_MF1.25_FLT) were implanted
297 to the bilateral prefrontal cortices (A-P 1.7, M-L ±0.5, D-V 0.5). To fit the shape of prefrontal, motor, and
298 insular cortex, customized 32-tetrode bundles were split into one or two clusters. To record the single
299 unit, electrodes were implanted in the left hemisphere with the following designs and coordinates:
300 silicon probe (A1x32-Edge -5mm-25-177-CM32) was implanted at the pIC (A-P −0.5-(-1.5), M-L 3-4, D-V
301 3); silicon probe (A1x32-5mm-25-177-CM32) was implanted at the aIC (A-P 1.5-1.7, M-L 2.5-3.5, D-V
302 2.5); silicon probe (A4x8-Edge-2mm-100-200-177-CM32) based opto-electrode was implanted at the
303 dmPFC (A-P 1.0-1.7, M-L 0.1-1.5, D-V 1); 32-tetrode bundles (one-cluster) based opto-electrode was
304 implanted at the dmPFC (A-P 1.0-1.7, M-L 0.1-1.5, D-V 1); 32-tetrode bundles (two-cluster) were
305 implanted at the pIC (A-P –0.5-(-1.5), M-L 3-4, D-V 3) and motor cortex (A-P 1-2, M-L 1-2, D-V 0.5).
306 During the surgery, the skull was horizontally aligned through a fixing apparatus (Stoelting Co.). An
307 anchor screw was placed on the right cerebellum to connect ground wires of the electrodes. After
308 placing the anchor screw and electrodes, silicone sealant (kwik-cast, world precision instrument) was
309 applied above the exposed brain tissue. A customized head bar
310 (github.com/ywang2822/Multi_Lick_ports_behavioral_setup) was then positioned over the skull. To
311 affix the implant, Metabond (C&B Metabond, Parkell) and dental cement (Lang Dental) were applied.
312 The behavioral experiments started at least one week after the surgery.

313 **Behavioral details**

314 The head-fix setup was connected to a construction rod (Throlabs) by a 3d printed connector
315 (github.com/ywang2822/Multi_Lick_ports_behavioral_setup). Multi-lick-ports
316 (github.com/ywang2822/Multi_Lick_ports_behavioral_setup) were placed in front of the head fix and
317 connected to the Dual Lick Port Detector (www.janelia.org/open-science/dual-lick-port-detector). Three
318 Clearlink sets (Baxter) were used for liquid delivery. The delivery speed was manually calibrated to 0.15 -
319 0.2mL min^{-1} every time before the behavioral test. The delivery switch was controlled by three solenoid
320 valves (LFVA1220210H, THE LEE CO.) in a noise-reducing box. The switch timing was programmed
321 through the Bpod (Sanworks). The signal of mice locomotor activity was collected through an optical
322 shaft encoder (H5-360-IE-S, US digital). For facial videography set-up, the camera (S3-U3-91S6C-C,
323 Teledyne FLIR) was positioned at the right side of the mouse's lateral face surface, which illuminated by
324 two infrared arrays. For laser delivery, a solid-state laser (Shanghai Laser& Optics Century Co., 473 nm)
325 was connected to fiber optic patch cord (Doric Lenses), which attached to the implanted optic fibers

using ceramic mating sleeves. To conditionally control the laser delivery by water, sucrose, or quinine onset, we used a 4-way data switch box (BNC, Kentek) to bridge the laser and solenoid valves. A programmable stimulator (A-M system, model 4100) was used to control laser delivery and a voltage pulse for tail shock experiment. All signals, including frame timing, wheel speed, liquid delivery timing, lick timing, shock timing, and laser delivery timing, were sent to an USB interface board (Intan Technologies, RHD).

For licking task, the deprivation was conducted until the body weight decreased approximately 22% (the deprivation time was 16 to 36 hours, varied from mouse to mouse). During training phase, mice learned to sense the water through their whiskers. We considered mice to become proficient at the task when licking happened within 3s after the delivery onset (DO) in all repeated trials. During the test phase, we first delivered water and 20% sucrose in a random sequence for a total of 30s. After at least 5 min, we then orderly delivered water, 20% sucrose, and 5 mM quinine for 10s each or water and 5 mM quinine for 15s each.

For tail shocking task, 16-23 volts electrical shocks were administered to the tail by a customized shocker (electric shock box machine kit, STEREN). Two conductive adhesive copper tapes were connected to the shocker and positioned 2 cm apart at the tail by sticking on customized heat shrink tube (various on the circumference of mouse tail). During the first time of training, the voltage of electrical shocks were adjusted until escaping behavior was observed (speed>10 cm s^{-1} right after the shock). This voltage was recorded and used for the following tests. Those who did not perform escaping behavior were excluded from the test.

Spike sorting and firing rate estimation

Before spike sorting, single unit data were acquired from 32-channel RHD head stage, which connected with a signal acquisition system (USB board, Intan Technologies) with sampling rate at 20 kHz. All spike sorting procedures were performed with an offline software Spikesorter [30, 31, 32] (swindale.ecc.ubc.ca/home-page/software/) under following parameters: (0.5 kHz and 4 poles high pass Butterworth filter) for signal filtering, (noise calculation: median; threshold: 80µV, 5x noise, 0.75ms window width) for even detection, and (pca dimensions = 2; template window: -0.8 to 0.8; starting sigma = 5; threshold = 9) for clustering. We used Bayesian adaptive kernel smoother [33] with following parameters, $\alpha = 4$ and β = (number of spike events) ^ (4/5), to estimate the firing rate of sorted spikes. For small scale temporal window (180ms), we used a bandwidth of 5ms. While for large scale temporal window (5s), we used a bandwidth of 200ms.

Optogenetic silencing

We illuminated bilateral prefrontal cortices using 473 nm laser to activate stGtACR2 [21]. Laser pulses (40ms width at 20Hz) were delivered in a 5s duration. The onset of laser pulses was triggered based on either water DO or quinine DO. The optogenetic silencing experiments were only performed after mice reached stable behavioral level (after at least two test phases and (lick onset (LO) – DO < 3s) in all test phases). The trials, of which licking frequency > 0.5 Hz in the time course 3s before DO, were excluded. Histological characterizations were used to identify the viral infection.

Opto-tagging

365 We applied laser pulses (1ms width at 20 Hz, 3s duration) on the unilaterally prefrontal cortex of viral
366 (AAV-ChR2) injected mice. Laser and network-evoked spikes (see also **Spike sorting and firing rate**
367 **estimation**) were identified using the Stimulus Associated spike Latency Test (SALT[19]). Specifically, laser
368 and network-evoked spikes were assessed in a 0-5ms and a 6-10ms temporal window after laser onset,
369 respectively. For those units with significant correlation (correlation coefficient > 0.85) of average
370 waveform and significantly different distribution ($P < 0.05$) of spike latency with baseline units were
371 identified as laser or network-evoked units.

372 **Chemogenetic inhibition**

373 Viral pAAV-hsyn-DIO-hm4D(Gi) (Addgene_44362-AAV5) injected mice were administered
374 intraperitoneally with Clozapine N-oxide dihydrochloride (CNO, 2mg kg^{-1}, Tocris) ten minutes before the
375 licking or tail shocking task. Only the mice reached stable behavioral level (after at least two test phases
376 and (LO – DO < 3s) in all test phases) were used for chemogenetic experiments. In the licking task, mice
377 were re-trained to lick the water one to two times after recovery from CNO administration. The re-
378 trained phases were not included in test phases.

379 **Analysis of facial and locomotor activity**

380 We collected the frames during the licking or tail shocking task. We then converted these frames into
381 histogram of oriented gradients (HOG) vectors by using 8 orientations, 32 pixels per cell and 1 cell per
382 block. To extract the most variant facial part, we cropped the ear part with 364x296 pixels fixed size and
383 manually selected position of each transformed HOG vector [20]. Temporally adjacent HOG vectors were
384 paired, the facial activity at each time point was calculated as follows: $1-\Delta R$, where ΔR is the correlation
385 coefficient between two temporally adjacent HOG vectors.

386 The signals that collected from the encoder were digital pulses. The locomotor activity was calculated as
387 speed (cm s^{-1}): $\frac{circumf}{CPR \cdot dt}$, where *circumf* is the circumference (cm) of the wheel, *CPR* (cycles per
388 revolution) is 360, and *dt* is the time interval between two digital pulses.

389 **Analysis of licking initiation/termination bias**

390 With the feeling of extremely thirsty, the mice will start a non-stop licking behavior when water is
391 available until feeling satiated or the delivery stopped [7] (**Supplementary Fig. 1d**). To evaluate if the mice
392 start or stop the continuous, but not discrete, lick, we calculated the initiation and termination bias. We
393 first calculated simple moving averages (SMAs) after water or quinine DO as following: $SMA = \frac{\sum_{i=1}^{n} l_i}{n}$,
394 where *l* is the lick times during a 200ms time window and $n = 5$. For the initiation bias, all values of
395 SMAs were ignored if there was a zero value after DO. We created a vector that contained SMAs
396 sampled at 200ms intervals. The SMA value was counted from the last non-zero value. The initiation bias
397 (ibias) was calculated as: $ibias = \frac{1}{idx}$, where *idx* is the first time point of the SMA > 1.2 (6Hz). If all SMA
398 values equal zeros in 6 seconds, *ibias* was set as zero. For the termination bias, the SMA value was
399 counted from the first time point after the quinine DO (for the water-quinine and water-sucrose-quinine
400 session) or the end time point of water delivery (for the session water-water session) or sucrose delivery
401 (for the session water-sucrose session). The termination bias (tbias) was calculated as: $tbias = \frac{1}{idx}$,
402 where *idx* is the first time point of the SMA < 1 (5Hz). If all SMA values ≥ 1, *tbias* was set as zero.

Cell classification

For the cell classification to discriminate water- and quinine-licks, we categorized single-units into four separate groups of neural representation (lick, positive valence (PV), negative valence (NV), and mixed valence (MV)) based on firing rate estimation at the lick window (LO-100ms: LO+80ms). To determine if the firing rate is significantly higher than normal condition, we created pseudo-trials that have the same lick interval with the corresponding real licks during the 10s baseline. Individual time bins of each pseudo lick trials were concatenated horizontally and shuffled. This procedure was repeated 1000 times and the pseudo-trial matrix was calculated as the mean among shuffled datasets. For real lick trials, we only selected the first four trials for encoding analysis. At each individual time bin of pseudo and real trials, we calculated Euclidean norm of two temporally adjacent firing rate estimations (5ms each). When absolute z-scores of two distributions ($z_{12} = \frac{\mu_1 - \mu_2}{\sqrt{\sigma_1^2 + \sigma_2^2}}$, where μ and σ represent mean and standard deviation, respectively, of the distribution1 and 2) exceeded 1.29, they were considered significantly different. We selected single-units with significantly high firing rate in water or quinine lick trials for further analysis. To evaluate the time bias of firing rate across lick trials, we mean centered the whole firing rate matrix. The Frobenius norms were calculated as follows: $norm = \sqrt{\sum_{i=1}^{n}(t_i - c)^2}$, where t_i is the mean column value of firing rate matrix with 10ms time bin across lick trials, *c* is centered mean, and n equals the number of time bins. We categorized a single-unit with the time bias of lick trials when its real norm greater than 95% of 1000 shuffled norms. To estimate if the peak of firing rate of two distributions is different, we compared the times of the maximum firing rate across lick trials between two distributions using two sample t-test. Their firing rate peaks were considered different when p-value less than 0.05 (z-score>1.64). Single-units were categorized into the group of lick, positive or negative valence, or mixed response when their firing rates met following conditions: lick, quinine trials > pseudo trials & water trials > pseudo trials & without time bias of the firing peak between quinine trials and water trials & with the time bias of water and quinine trials; positive valence (PV), water trials > pseudo trials & water trials > quinine trials & quinine trials ≤ pseudo trials; negative valence (NV), quinine trials > pseudo trials & quinine trials > water trials & water trials ≤ pseudo trials; mixed valence (MV), water trials > pseudo trials & quinine trials > pseudo trials & with time bias of the firing peak between quinine trials and water trials & with the time bias of water and quinine trials; others were grouped into unrelated valence (UV).

To examine if there is a trial bias of firing rate during the water-licks, we compared the spike times at the small scale time window of water-licks. The matrices were binned (8 trials per group) and the mean values of each group were calculated. New generated binned firing rate matrices were then used. We next calculated Frobenius norm: $\sqrt{\sum_{i=1}^{n}(t_i - c)^2}$, where t_i is the mean row value of the binned firing rate matrix, *c* is centered mean, while *n* is the number of trials. When the real Frobenius norm was greater than 95% of 1000 shuffled norm, the single-unit was considered with trial bias in water-lick trials.

For the cell classification to discriminate initial and terminal phase of persistent movement, we assessed the firing rates at the 2s temporal window before or after the first water LO or quinine DO. The Five time point (0s, 0.5s, 1s, 1.5s, and 2s) were used for classification analysis. To construct pseudo data, the over 70s spike train data were used to extract five-time point random temporal window. We defined a single-unit with estimated firing rate higher than 65% pseudo data at the temporal window (1st water LO-2s: 1st

water LO) and lower than 35% pseudo data at the temporal window (quinine DO: quinine DO+2s) as initial phase neural representation before LO; with estimated firing rate higher than 65% pseudo data at the temporal window (1st water LO: 1st water LO+2s) and lower than 35% pseudo data at the temporal window (quinine DO: quinine DO+2s) as initial phase neural representation after LO; with estimated firing rate higher than 65% pseudo data at the temporal window (quinine DO: quinine DO+2s) and lower than 35% pseudo data at the temporal window (1st water LO-2s: 1st water LO+2s) as terminal phase neural representation. Others were classified as neural representations of unrelated movement phases.

Connectivity estimation

To estimate the connections among different neural representations, we used Total Spiking Probability Edges (TSPE [18]). This method allows us to calculate the cross-correlation between pairs of spike trains and to evaluate excitatory connections. Furthermore, it gives high accuracy estimation in a short recording period. However, this method can only be used for the comparison of two individual single-units. To apply this method on two networks, we first selected spike trains of photo-tagged and network evoked single-units. We assumed the connection from photo-tagged to network evoked single-units is positive. For the individual single-unit, 3s time duration of spike times data was cropped and sent to TSPE calculation. We next selected spike trains of the neural representations of NV, PV, and initial phase in three brain regions (IC, M1, and dmPFC). Individual time windows of 180ms across the lick trials (LO-100ms: LO+80ms) were extracted and recombined. The connectivity among these neural representations was calculated using TSPE. To perform a statistical test, we compared the real TSPE and the pseudo TSPE, in which 3s spike times data were shuffled 200 times and created pseudo spike times. 70, 80, 90, 95, and 99 percentile of pseudo TSPE were used for the comparison based on the neural representation number of real data. Specifically, if the real data number is less than 10, they will not be used for the comparison; if the real data number is between 10 and 15, 80 percentile of pseudo TSPE will be used for the comparison; if the real data number is between 15 and 20, 90 percentile of pseudo TSPE will be used for the comparison; if the real data number is between 20 and 32, 95 percentile of pseudo TSPE will be used for the comparison; if the real data number is larger than 32, 99 percentile of pseudo TSPE will be used for the comparison.

Decoding analysis

For both small and large scale temporal window decoding, we employed a multiclass linear discriminant analysis. We first estimated spike firing rate (see **Spike sorting and firing rate estimation)** in water and quinine lick window (LO-100ms to LO+80ms for small scale window and first LO-2s to first LO+3s for large scale window). The firing rate was normalized by dividing the maximum firing rate value of water and quinine lick window. To create firing rate pseudo data, pseudo LOs were randomly selected for the entire time duration of the spike train. This procedure was repeated 50 times. Same with real data normalization, the pseudo data were divided by the max firing rate value in each repeat. To improve the subsequent decoding performance, we reduced the dimensionality of the neural activity by PCA. The dimensions that explained over 85% of the data variance were selected to train a decoder, which is based on an error-correcting output codes (ECOC) classifier using binary support vector machine (SVM) learner (MATLAB ‘fitcecoc’ function). 50 percent of real and pseudo data were used to train the decoder, and the rest of them were used to test the decoder's performance. This procedure was repeated 10 times to get an average accuracy and standard deviation.

Facial activity prediction

We trained Hammerstein-Wiener model to predict behavioral activity using estimated firing rate [34]. Before the modeling, the firing rates were estimated in a large scale temporal window (first LO-2s to first LO+3s) and normalized into a range from 0 to 1 by dividing the maximum firing rate value of water and quinine lick window. Empty and zero firing rates vectors were removed. The facial dynamics (see **Facial activity analysis**) were smoothed using Gaussian filter. The parameters that can best simulate facial dynamics were used to construct Hammerstein-Wiener model. Specifically, the number of zeros was set in a range from 0 to 2 (nb-1); the number of poles was set in a range from 1 to 3 (nf); and the degree of input nonlinearity estimator (one-dimensional polynomial) was set from 2 to 5. We then used MATLAB function 'predict' to obtain decoding accuracies of facial dynamics from the test spike data. Specifically, the data (four trials in total) were split 50/50. First two trials were used for training the model and last two trials were used for testing. To avoid and overflow error, the values which lower than negative 1500 were excluded.

Histology

To check the position of implanted electrodes and site of injection, mice were anesthetized with 2% isoflurane (v/v) and perfused intracardially with 0.9% saline followed by 4% paraformaldehyde (PFA). Fixed brains were washed three times before dehydration in 30% sucrose for 24 hr. Slices were cut on a cryostat (MICROM, HM505E) at 70μm thickness after embedding with an optimal cutting temperature compound (Tissue tek). Fluorescent images were acquired by an LSM 980 microscope (Zeiss), with a 10 × 0.45NA objective or a 2.5 × 0.085NA objective.

MP network-based model

The purpose of this modeling was to create lick raster readouts through giving a type of current input, simulating a network of neural activities, and transforming the simulated spike timing to the lick timing.

For the input current, we set the starting time $\boldsymbol{t_s}$ with a flexible (1-200ms) or a fixed (50ms) delay after the DO. The amplitudes of input current were varied from 50-200pA according to the different simulations. To test the effect of input continuity, the current was cut using one or twice 200ms zero amplitude.

We simulated neural activity using Brian2 simulator package in a customized python code based on a sparsely connected spiking neuron network [35]. The network consisted of 1000 excitatory and 800 inhibitory neurons as default (we decreased this number in the simulation of optogenetic inhibition). The membrane potential of each neuron was modeled according to the MP neuron membrane properties [17] based on the Hodgkin-Huxley model as following:

$$\frac{dV}{dt} = \frac{gl\cdot(El-V)-g_{Na}\cdot m^3\cdot h\cdot(V-E_{Na})-g_K\cdot n^4\cdot(V-E_K)+g_e\cdot(E_e-V)+g_i\cdot(E_i-V)+I_{ex}\cdot t_s}{C_m},$$

$$\frac{dg_e}{dt} = -\frac{g_e}{\tau_e},$$

$$\frac{dg_i}{dt} = -\frac{g_i}{\tau_i},$$

where the excitatory and inhibitory synaptic time constants $\boldsymbol{\tau_e}$ and $\boldsymbol{\tau_i}$ were set as 5 and 10ms, respectively. Other metrics were adjusted to adapt the inter-spike-intervals of L5 mPFC MP neuron, which proposed to be a functional and dominate interneurons that bridge the gap between deep brain

regions and motor cortex [17]. The membrane potential $\boldsymbol{V}$ was initiated randomly at a range from -65mV to -63mV. The excitatory conductance was set at a range from 0 to 0.06ns and the inhibitory counterpart was in 0 to 1.5ns.

The synapse action was dependent on the usage u and availability x of released neurotransmitter before and after an action potential as following: $\frac{du}{dt} = -\omega_f \cdot u, \frac{dx}{dt} = \omega_d - \omega_d \cdot x$, where the facilitation rate was set as 3.33 s^{-1} and the depression rate was set as 2 s^{-1}. The rest synaptic release probability was set as 0.6. The probability of excitatory connection of the network was given as 0.1 and the inhibitory counterpart was 0.2.

To generate lick raster data from the network, we first assumed that one single lick cycle is governed by a rotational neural dynamic [25]. Then we divided one cycle of the lick into nine phases. The triggering probability *P* of a lick signal was calculated from the network through a decision algorithm:

$$P(t) = \begin{cases} 1, \ \prod_{\theta=0}^{2\pi}(\sum_{i=1}^{N} \varphi_{\theta i}(t-280)) > 0 \ \& \ S\left(\sum_{i=1}^{N} \varphi_{\theta i}(t-280)\right) < 30 \\ 0, \ \prod_{\theta=0}^{2\pi}(\sum_{i=1}^{N} \varphi_{\theta i}(t-280)) = 0 \ or \ S\left(\sum_{i=1}^{N} \varphi_{\theta i}(t-280)\right) \geq 30 \end{cases},$$

where *S* represents the standard deviation of the spike counts in whole phases.

Statistical test

For comparison of the mean of facial and locomotor activity (**Supplementary Fig. 1k-n** and **Supplementary Fig. 9e, h**), comparison of the mean of licking frequency at different sessions (**Supplementary Fig. 1c-f**), and comparison of TSPE (**Supplementary Fig. 5**), we used two-tailed Wilcoxon signed rank test. For evaluation of the slope of spike counts trend line, we used one sample t test (**Supplementary Fig. 4e**). The rest of statistical tests were two sample t test.

DATA AVAILIBILITY

The raw data that support these findings are available from corresponding author upon reasonable request. Source data are provided with this paper.

CODE AVAILIBILITY

Materials and setup instruction for head fix and triple lick ports are freely available (https://github.com/ywang2822/Multi_Lick_ports_behavioral_setup). Spike extraction used SpikeSorter (swindale.ecc.ubc.ca/home-page/software). Connectivity estimation used TSPE toolbox (https://github.com/biomemsLAB/TSPE). Estimated firing rate using Bayesian adaptive kernel smoother (https://github.com/nurahmadi/BAKS). Identified opto-tag single-units using stimulus-associated spike latency test (http://kepecslab.cshl.edu/software/). Cartoonish mice were created using Biorender (biorender.com). Venn diagrams were plot using a customized Matlab script (https://www.mathworks.com/matlabcentral/fileexchange/22282-venn). Other customized codes are available from https://doi.org/10.5281/zenodo.7953792.

558 **Figure Legends**

559 **Fig 1. Dissociable neural representations of movement phases and valence**

560 **a.** Schematic of the experimental setup. Water or quinine was continuously delivered through a multi-
561 lick-ports with a time delay of zero at the delivery switches. Mice were trained to respond the liquid
562 delivery without conditioning. **b.** Schematic of recording sites. IC, insular cortex; dmPFC, dorsal medial
563 prefrontal cortex; M1, primary motor cortex. **c.** A representative task of persistent lick. Two recording
564 windows were selected near the water or quinine delivery onset (DO). For the large scale window (L-
565 window), the recording epoch began 2 seconds before the 1st water or quinine lick onset (LO) until 3
566 seconds after the first water or quinine LO. For the small scale window (S- window), the recording epoch
567 began from 100 ms before the LO to 80 ms after the LO. **d.** Spike raster and firing rate estimation of four
568 representative single- units classified to represent the initial phase and terminal phase of persistent
569 movement, positive valence (PV), and negative valence (NV) in the L- window and S- window,
570 respectively. Spike raster and firing rate under water and quinine licks are colored blue and red,
571 respectively. **e.** Pie chart showing the percentage of the classified neural representations. **f.** Venn
572 diagram of the neural representations of valence and movement phases. Percentages of each category
573 in all recorded neurons are shown in the diagram.

574 **Fig 2. Coding of initial phase in dmPFC MP neurons**

575 **a.** Schematics showing the labeling and recording of MP neuron in dmPFC. **b.** Representative image
576 showing channelrhodopsin-2 (ChR2) expression in MP neuron. **c.** Identification of labeled MP neuron.
577 We identified the unit as MP neuron when there was a significant probability of evoked spikes,
578 appeared from 0 to 5ms after laser onset (light blue), and when there was a high correlation (R>0.85)
579 between evoked spikes (light blue waveform) and other spikes (black waveform). **d & g.** Color-coded
580 plot showing MP neural response in S-window (d) and in L-window (g) from one representative trial. **e &**
581 **h.** Fraction of valence (e) and movement phases (h) classified neural representations in MP and IC
582 neurons. **f & i.** Left, PCA trajectories of dmPFC MP neuron. Right, bar plot showing cumulative variance
583 explained percentage of first two PCs. **j** Comparison of mean Euclidean distance from all PC dimensions
584 of dmPFC MP neurons, between S-window and L-window. Values are mean ± s.e.m. **k.** Decoding of taste
585 signals (water or quinine) in S-window (left) phase (initial or terminal) in L-window (right). **l.** Examples of
586 facial activities (black traces) overlaid with MP firing predictions (Left, initial phase; right, terminal
587 phase). **m.** Summary of facial activity predictions by recorded MP neurons. *P < 0.05, **P < 0.01, ****P
588 < 0.0001, n.s. p > 0.05.

589 **Fig 3. dmPFC MP neuron is required for the initiation of persistent licking movement**

590 **a.** Left: schematic of bilateral silencing MP neurons in dmPFC. Right: experimental design for
591 optogenetic silencing. Mice received laser or sham stimulation (5s, 20Hz) concurrent with water or
592 quinine DO. **b & d.** Raster plot showing licking movement relative to water DO (b) or quinine DO (e).
593 Laser (left) or sham (right) was triggered by DO. Cyan background and dash box represent laser (b) and
594 sham (d) delivery period, respectively. **c & e.** Percentage of bias that started (c) or stopped (e) persistent
595 lick (see Methods). **f.** Color-coded plot showing facial activity relative to water DO. **g.** Z scored facial
596 activity relative to water DO. Values are mean ± s.e.m. *p<0.05, n.s. p>0.05.

597 **Fig 4. Silencing of dmPFC MP neuron impairs the neural activity in motor and insular cortex**

598 **a.** Schematic of bilateral silencing MP neurons in the dmPFC. **b & c.** Schematic of recording sites in IC (b)
599 and M1 (c). **d & e.** Baseline subtracted, z scored firing rate, relative to water DO, for the recorded
600 neurons in IC (d) and in M1 (e) from one representative trial. Cyan background and dash box represent
601 laser (top) and sham (bottom) delivery period, respectively. **f & g.** Mean baseline subtracted, z scored
602 firing rate, relative to water DO, of IC (f) and M1 (g) neurons. Values are mean ± s.e.m. *p<0.05.

603 **Fig 5. Modulation of neuron number and input in the MP network-based computational model**

604 **a.** The MP network-based model. A spiking network receives an input of current after the DO (delivery
605 onset) with a flexible (1 to 200ms, for panel B) or fixed (50ms, for panel C) delay. 56% connectivity is
606 excitatory and 44% of it is inhibitory. The lick raster outputs are calculated by a decision algorithm (see
607 Methods) using the simulated spike data. **b.** Simulation of optogenetic inhibition of dmPFC MP neurons
608 by reducing the neuron number (both excitatory and inhibitory neurons) in the MP network based
609 model. Left 1-3: lick raster produced by the model under indicated neuron number. Right: percentage of
610 initiation bias that calculated from left lick raster data. **c** Performance of licking behavior under the
611 different continuities of input current. Left 1-3: top: lick raster plots under, bottom: inputs with
612 indicated interruption times. Right: percentages of initiation bias with indicated interruption times. *p <
613 0.05, ****p < 0.0001

614 **Fig 6. Summarized model for how dmPFC MP neurons initiate persistent movement.**

615 **a.** Pattern of neuronal activation during the persistent licking movement. After the onset of stimulation,
616 there is a delay of approximately 1.3 seconds until the first lick onset. In the initial phase (the licking
617 frequency is driven to the maximum), the indicated three types of neurons are activated. In the
618 persistent phase, dmPFC MP neurons are inactivated, while M1 and IC neurons show persistent activity.
619 **b.** During the initial phase, when the sensory signals are received, dmPFC MP neurons activate
620 themselves and the downstream motor neurons. The latter drive the licking movements that bring the
621 tongue into contact with the water. The taste signal from the tongue is further transmitted to the
622 valence-encoding neurons in the IC. During the persistent phase, no signal is transmitted from the
623 dmPFC MP neurons to the motor neurons, but the motor neurons is continuously activated. This results
624 in persistent licking movement and persistent valence encoding in the IC.

625 **Supplementary Fig 1. Behavioral performance in persistent licking tasks**

626 **a.** Schematic of timeline for licking tasks per trial. **b.** Schematic of behavioral setup and equipment. **c-f.**
627 Lick behavior relative to delivery onset (DO, left) and to 1st lick onset (LO, right) after DO in four sessions.
628 Top, raster plots showing lick behavior in the session water (w, 15s)-quinine (q, 15s) (c), water (w, 15s)-
629 water (w, 15s) (d), water (w, 15s)-sucrose (s, 15s) (e), and water (w, 10s)-sucrose (s, 10s)-quinine (q,
630 10s). Bottom, lick frequency plot. The 'peak' indicates the maximum lick frequency. Wilcoxon signed-
631 rank test, in comparison with baseline: ****p<0.0001, n.s. not significant. Values are mean ± s.e.m. **g.**
632 Comparison of the percentage of body weight decrease among four sessions using one-way anova. **h &**
633 **i.** Percentage of bias that started (h) or stopped (i) persistent lick (Methods). One-way anova: p=0.1147
634 for initiation bias; p<0.0001 for termination bias. Bonferroni multi-compare: **p<0.01 ****p<0.0001. **j.**
635 Illustration of calculating facial activity as 1-Δcorrelation (see Methods). **k-n.** Color-coded plot and traces
636 showing facial and locomotor activity relative to water DO. We compared the epochs from DO to LO,
637 from switch onsets to switch onsets+5s, from end onsets to end onsets+5s with the baseline. Wilcoxon
638 signed-rank test: *p<0.05, **p<0.01, ***p<0.001, ****p<0.0001, n.s. not significant. Values are mean ±

s.e.m. **o-s.** Comparison of licking performance (o), facial and locomotor activity (p and q), initiation bias (r), and termination bias (s) between male and female mice in w-q session. *p<0.05, **p<0.01, ***p<0.001, ****p<0.0001, n.s. not significant. Values are mean ± s.e.m.

Supplementary Fig 2. Histological and electrophysiological verification

a. Histological verification of IC implant sites. From left to right: representative images of anterior IC implant is shown in 1st to 2nd columns and posterior IC implant is shown in 3rd to 4th columns. The magnified images are shown2nd and 4th columns. **b.** Histological verification of M1 implant sites. From left to right: representative anterior M1implant is shown in 1st to 2nd columns and posterior M1 implant is shown in 3rd to 4th columns. The magnified images are shown in 2nd and 4th columns. **c.** Histological verification of optic fiber implans for optogenetic silencing in bilateral dmPFC. **d.** Histological verification of viral injections for chemogenetic inhibition of hM4D labeled neuron in bilateral dmPFC. **e.** Histological verification of viral injections and electrodes and optic fiber implants for optogenetic identification of ChR2 labeled neuron in unilateral dmPFC. **f.** Electrophysiological verification of photo-tagged and network-excited neurons (see Methods).

Supplementary Fig 3. Analysis of single-unit classification

a. Procedure for shuffling baseline data. Left: color coded firing rates in the real and pseudo lick trials (the pseudo lick number equals to the real lick number after the baseline). Right: distributions of mean adjacent Euclidean norm obtained from the 1000 pseudo datasets and 1 real dataset. **b.** Procedure for categorizing the single-units with or without time bias. Top: example of a single-unit with time bias. Bottom: example of a single-unit without time bias. Left: color-coded firing rates showing shuffled data during lick trials. Middle: real data firing rates. Right: distributions of Frobenius norms of shuffled data. The single-unit was categorized as time bias when its Frobenius norm higher than 95 percentile of shuffled data. **c.** Spike raster and firing rates plots showing representative classified single-units that encode lick, mix valence (MV), negative valence (NV), and positive valence (PV) in the session water-quinine (wq, top) and the session water-sucrose-quinine (wsq, bottom). Black dots denote the peak firing rate at the each lick trial. **d.** Procedure for categorizing the neural representations with or without water-lick trial bias. Example of a single-unit with (top) or without (bottom) lick trial bias (matrix was binned with each 8 trials). Left: color-coded firing rates showing shuffled data during water-lick trials. Middle: real data firing rates. Right: distributions of Frobenius norms of shuffled data. The single-unit was categorized as water-lick bias when its Frobenius norm higher than 95 percentile of shuffled data. **e.** Color-coded firing rates showing the two examples of PV neural representations with (right) or without (left) water-lick trial bias. **f.** Procedure for generating pseudo data. Left: illustration of pseudo data selecting. Right: distributions of firing rates in 5 pseudo time points. **g.** Example of a single-unit firing rate in three recording epochs. **h.** Spike raster and firing rates plots showing representative classified single-units that represented initial phase-after lick onset (ALO), initial phase-before lick onset (BLO), terminal phase, and mixed phase (MG).

Supplementary Fig 4. The percentage and firing trend of specific neural representations in the brain regions IC, M1, and dmPFC

a-c. Percentage of the classified neural representations in IC (a), M1 (b), and dmPFC (c). **a1** & **b1** & **c1**: percentage of PV, NV, MV, lick, and UV (unrelated valence) neural representations. **a2** & **b2** & **c2**: percentage of initial phase (including ALO and BLO), terminal phase, mixed phase, and unrelated

movement phase neural representations. **a3** & **b3** & **c3**: venn diagram showing the overlap and non-overlap percentage of indicated neural representations. **d.** The spike counts of indicated neural representations during water-licks. A blue dot denotes the spike times in the small scale window (LO-100ms to LO+80ms) of a water-lick trial. Blue lines represent the trend line of blue dots. **e.** Slopes of trend line of overall non-overlapping neural representation groups in IC, M1, and dmPFC as indicated. The symbol + and – represent the significant positive and negative value of its labeled trend line slope, respectively. + or - $P<0.05$, one sample t-test.

Supplementary Fig 5. The connectivity among specific neural representation groups

a-b. Connectivity of neural pairs between photo-tagged and network-excited single-units. A: Cross-correlograms of individual neural pairs. B: TSPE comparison of real data and the shuffled data at different percentile. P values are measured by Wilcoxon signed-rank test. **c-d.** Connectivity among classified neural representations. **Left:** Cross-correlograms of individual neural pairs. **Right:** TSPE comparison of real data and the shuffled data at 99 percentile. All mean of real TSPEs are less than mean of 99% shuffled data.

Supplementary Fig 6. The decoding of liquid types in IC, M1, and dmPFC along with lick proceeding

a1 & b1 & c1. Decoding of the water-licks in 1st recording epoch (water DO to water DO+15s) and in 2nd recording epoch (water DO+15s to delivery end). **a2 & b2 & c2.** Decoding of the water-licks in 1st recording epoch (water DO to water DO+15s) and the 1st sucrose-lick in 2nd recording epoch (sucrose DO to delivery end). **a3 & b3 & c3.** Decoding of the water-licks in 1st recording epoch (water DO to water DO+15s) and the 1st quinine-lick in 2nd recording epoch (quinine DO to delivery end). **From left to right:** 1st column, color-coded plot showing z scored neural response in the first lick window of 1st recording epoch and 2nd recording epoch; 2nd column, decoding of the first water-lick in 1st recording epoch and in 2nd recording epoch; 3rd column, color-coded plot showing neural response in the 42th lick window of 1st recording epoch and in the 1st lick window of 2nd recording epoch; 4th column, decoding of the 42th water-lick in 1st recording epoch and the first lick in 2nd recording epoch. 5th column, different brain regions showing different liquid type discrimination and changing the discrimination level (decoding performance) along with lick trials evolving. Decoding of water-licks (from 1st to 42th lick trial) in 1st recording epoch and first lick in 2nd recording epoch. Values are mean ± s.e.m.

Supplementary Fig 7. The decoding of initial versus terminal phase in IC, M1, and dmPFC

a1 & b1 & c1. Decoding of the initial phase in 1st recording epoch (1st water LO-2s to 1st water LO+3s) and the terminal phase in 2nd recording epoch (water delivery end-2s to water delivery end+3s). **a2 & b2 & c2.** Decoding of the initial phase in 1st recording epoch (1st water LO-2s to 1st water LO+3s) and the terminal phase in 2nd recording epoch (sucrose delivery end-2s to sucrose deliver end+3s). **a3 & b3 & c3.** Decoding of the initial phase in 1st recording epoch (1st water LO-2s to 1st water LO+3s) and the terminal phase in 2nd recording epoch (1st quinine LO-2s to 1st quinine LO+3s). **Top:** color-coded plot showing z scored neural response in the 1st recording epoch and 2nd recording epoch. **Bottom:** decoding performance. Values are mean ± s.e.m.

Supplementary Fig 8. Prediction of facial activity from spike activity in regions IC, M1, and dmPFC

a. Examples of facial activities (black traces) overlaid with Hammerstein-Wiener model using indicated parameters. **b-d.** Firing rate predictions of facial activity using Hammerstein-Wiener model. B1 & C1 &

720 D1: examples of facial activities (black traces) overlaid with firing rate predictions (right, water-lick; left,
721 quinine-lick). B2 & C2 & D2: summary of facial activity predictions. *p<0.05

722 **Supplementary Fig 9. Behavioral effect of dmPFC MP neuron chemogenetically silencing**

723 **a.** Schematic of bilateral silencing MP neurons in dmPFC. **b.** Lick behavior relative to DO with or without
724 CNO administration. From left to right: 1st column and 3rd column, raster plots showing lick behavior in
725 the session w (15s)-w or s (15s). 2nd column and 4th column, lick frequency plot. **c.** Comparison of lick
726 chance between saline and CNO administrated mice after water delivery. **d.** Comparison of the
727 percentage of body weight decrease between saline and CNO administrated mice. **e.** Color-coded plot
728 and traces showing z scored facial and locomotor activity relative to water DO. We compared mean
729 facial and locomotor activity in the epochs from DO to LO, from switch onsets to switch onsets+5s, from
730 end onsets to end onsets+5s with that in the baseline. Wilcoxon signed-rank test: *p<0.05, **p<0.01,
731 n.s. not significant. **f-g.** Comparison of z scored facial activity (f) and locomotor activity (g) between
732 saline and CNO administrated mice at various epochs as indicated. Two sample t-test: **p<0.01, n.s. not
733 significant. **h.** Color-coded plot and traces showing facial and locomotor activity relative to shock onset
734 (SO). The mean facial and locomotor activity in the epoch from SO to SO+5s were compared with that in
735 the baseline. Wilcoxon signed-rank test: *p<0.05, ****p<0.0001, n.s. not significant. **i.** Comparison of z
736 scored facial activity (top) and locomotor activity (bottom) between saline and CNO administrated mice
737 at the epoch SO to SO+5s. Two sample t-test: *p<0.05, ****p<0.0001.

738 **Supplementary Fig 10. Behavioral effect of dmPFC MP neuron optogenetically silencing**

739 **a1 & b1.** Top, raster plots showing Lick behavior relative to DO shining with or without laser. Bottom,
740 Color-coded plot and traces showing facial and locomotor activity relative to DO. Laser (left) or sham
741 (right) was triggered by DO. **c1 & d1.** Color-coded plot and traces showing facial and locomotor activity
742 relative to DO. Laser (left) or sham (right) was triggered by DO. Cyan background and dash box represent
743 laser and sham delivery period, respectively. **a2 & b2.** Left, lick frequency relative to DO. Right,
744 Comparison of lick times at laser or sham treatment periods. **a3 & b3 & c2 & d2.** Comparison of facial
745 (left) and locomotor (right) activity between laser and sham treatment periods. **a4 & b4 & c3 & d3.**
746 Comparison of the percentage of body weight decrease between laser and sham treatment groups. **c4.**
747 lick frequency relative to DO. The analyzing window was extended to full time period. No significant
748 difference between laser and sham treatment was found after laser off. Two sample t-test: n.s. not
749 significant **p<0.01

750 **Supplementary Fig 11. Comparison of the MP network based model and the experimental data**

751 **a.** Voltage responses of a representative MP neuron in the experiment (data from our previous work[17],
752 black traces) and the model (red traces) to step current injections. **b.** Tongue movement and MP
753 network is quantified by rotational phases. Left: representative image showing tongue movement.
754 Right: one cycle of MP network and tongue movement was set as 125ms and there was a 280ms delay
755 before the signal from MP network arrived to tongue. **c.** Polar histogram of experimental (top) and
756 simulated (bottom) network phases for indicated LO numbers. The blue area of each phase indicates the
757 relative spike counts. **d.** Neural activity of real (left, black) and simulated (right, red) MP network related
758 to lick frequency and initiation bias. Dash lines denote the 95% intervals. R-squares and P values of the
759 linear regression are labeled at each panel. In both **c** and **d**, the experimental data were only chosen

from the neurons that the normalized firing rate lower than 50 (65% of the total neuron number) given that slow spiking MP neurons are mainly functional linking deep brain regions and motor cortex[17].

REFERENCE

1. Ryans DG. An experimental attempt to analyze persistent behavior: I. measuring traits presumed to involve "persistence". *The Journal of General Psychology* **19**, 333-353 (1938).

2. Wolf TH. The effect of praise and competition on the persistent behavior of kindergarten children. *University of Minnesota Child Welfare Monograph Series*, (1938).

3. Grant AM, Campbell EM, Chen G, Cottone K, Lapedis D, Lee K. Impact and the art of motivation maintenance: The effects of contact with beneficiaries on persistence behavior. *Organizational behavior and human decision processes* **103**, 53-67 (2007).

4. Adolphs R, Anderson DJ. Building Blocks and Features of Emotions. In: *The Neuroscience of Emotion*). Princeton University Press (2018).

5. Zhou T*, et al.* History of winning remodels thalamo-PFC circuit to reinforce social dominance. *Science* **357**, 162-168 (2017).

6. Gibson WT*, et al.* Behavioral responses to a repetitive visual threat stimulus express a persistent state of defensive arousal in Drosophila. *Curr Biol* **25**, 1401-1415 (2015).

7. Allen WE*, et al.* Thirst regulates motivated behavior through modulation of brainwide neural population dynamics. *Science* **364**, 253 (2019).

8. Tovote P*, et al.* Midbrain circuits for defensive behaviour. *Nature* **534**, 206-212 (2016).

9. Jercog D*, et al.* Dynamical prefrontal population coding during defensive behaviours. *Nature* **595**, 690-694 (2021).

10. Beyeler A*, et al.* Organization of Valence-Encoding and Projection-Defined Neurons in the Basolateral Amygdala. *Cell Rep* **22**, 905-918 (2018).

11. Wang L*, et al.* The coding of valence and identity in the mammalian taste system. *Nature* **558**, 127-131 (2018).

12. Zhang X*, et al.* Genetically identified amygdala-striatal circuits for valence-specific behaviors. *Nat Neurosci* **24**, 1586-1600 (2021).

13. Li H*, et al.* Neurotensin orchestrates valence assignment in the amygdala. *Nature* **608**, 586-592 (2022).

14. Solomon RL. The opponent-process theory of acquired motivation: the costs of pleasure and the benefits of pain. *Am Psychol* **35**, 691-712 (1980).

15. Peng Y, Gillis-Smith S, Jin H, Trankner D, Ryba NJ, Zuker CS. Sweet and bitter taste in the brain of awake behaving animals. *Nature* **527**, 512-515 (2015).

16. Levy S*, et al.* Cell-Type-Specific Outcome Representation in the Primary Motor Cortex. *Neuron* **107**, 954-971 e959 (2020).

17. Wang Y, Sun QQ. A long-range, recurrent neuronal network linking the emotion regions with the somatic motor cortex. *Cell Rep* **36**, 109733 (2021).

18. De Blasi S, Ciba M, Bahmer A, Thielemann C. Total spiking probability edges: A cross-correlation based method for effective connectivity estimation of cortical spiking neurons. *J Neurosci Methods* **312**, 169-181 (2019).

19. Kvitsiani D, Ranade S, Hangya B, Taniguchi H, Huang JZ, Kepecs A. Distinct behavioural and network correlates of two interneuron types in prefrontal cortex. *Nature* **498**, 363-366 (2013).

20. Dolensek N, Gehrlach DA, Klein AS, Gogolla N. Facial expressions of emotion states and their neuronal correlates in mice. *Science* **368**, 89-94 (2020).

21. Mahn M*, et al.* High-efficiency optogenetic silencing with soma-targeted anion-conducting channelrhodopsins. *Nat Commun* **9**, 4125 (2018).

22. Rigotti M*, et al.* The importance of mixed selectivity in complex cognitive tasks. *Nature* **497**, 585-590 (2013).

23. Martin RE, Murray GM, Kemppainen P, Masuda Y, Sessle BJ. Functional properties of neurons in the primate tongue primary motor cortex during swallowing. *J Neurophysiol* **78**, 1516-1530 (1997).

24. Yao D, Yamamura K, Narita N, Martin RE, Murray GM, Sessle BJ. Neuronal activity patterns in primate primary motor cortex related to trained or semiautomatic jaw and tongue movements. *J Neurophysiol* **87**, 2531-2541 (2002).

25. Linden H, Petersen PC, Vestergaard M, Berg RW. Movement is governed by rotational neural dynamics in spinal motor networks. *Nature* **610**, 526-531 (2022).

26. van Aerde KI, Feldmeyer D. Morphological and physiological characterization of pyramidal neuron subtypes in rat medial prefrontal cortex. *Cereb Cortex* **25**, 788-805 (2015).

27. Poggio T, Bizzi E. Generalization in vision and motor control. *Nature* **431**, 768-774 (2004).

28. Bolkan SS*, et al.* Thalamic projections sustain prefrontal activity during working memory maintenance. *Nat Neurosci* **20**, 987-996 (2017).

29. Kaminski J, Sullivan S, Chung JM, Ross IB, Mamelak AN, Rutishauser U. Persistently active neurons in human medial frontal and medial temporal lobe support working memory. *Nat Neurosci* **20**, 590-601 (2017).

30. Swindale NV, Spacek MA. Spike sorting for polytrodes: a divide and conquer approach. *Front Syst Neurosci* **8**, 6 (2014).

31. Swindale NV, Spacek MA. Spike detection methods for polytrodes and high density microelectrode arrays. *J Comput Neurosci* **38**, 249-261 (2015).

32. Swindale NV, Spacek MA. Verification of multichannel electrode array integrity by use of cross-channel correlations. *J Neurosci Methods* **263**, 95-102 (2016).

33. Ahmadi N, Constandinou TG, Bouganis CS. Estimation of neuronal firing rate using Bayesian Adaptive Kernel Smoother (BAKS). *PLoS One* **13**, e0206794 (2018).

34. Ethier C, Oby ER, Bauman MJ, Miller LE. Restoration of grasp following paralysis through brain-controlled stimulation of muscles. *Nature* **485**, 368-371 (2012).

35. Brunel N. Dynamics of sparsely connected networks of excitatory and inhibitory spiking neurons. *J Comput Neurosci* **8**, 183-208 (2000).

ACKNOWLEDGEMENTS

We thank Dr. Z. Zhang for imaging and C. Zhang for animal husbandry, histology assistance and items purchasing. We thank O. Gonzalez for 3D printing and helps on behavioral set-up design. We thank Drs. K. Gerow, C. Jiang, M. Minear, and J. Dai for discussion. We thank Dr. N. Li for providing Bpod and Dual Lick Port Detector. This work is supported by grants from National Institute of Mental Health (1R21MH131363-01) and from National Institute of General Medical Sciences (2P20GM121310).

AUTHOR CONTRIBUTIONS

Q.S. supervised the project, acquired the funding, and edited the manuscript. Y.W. built the behavioral set-up, collected and analyzed data, performed the simulation, and wrote the original manuscript.

COMPETING INTERESTS

The authors declare no competing interests.

Fig 1

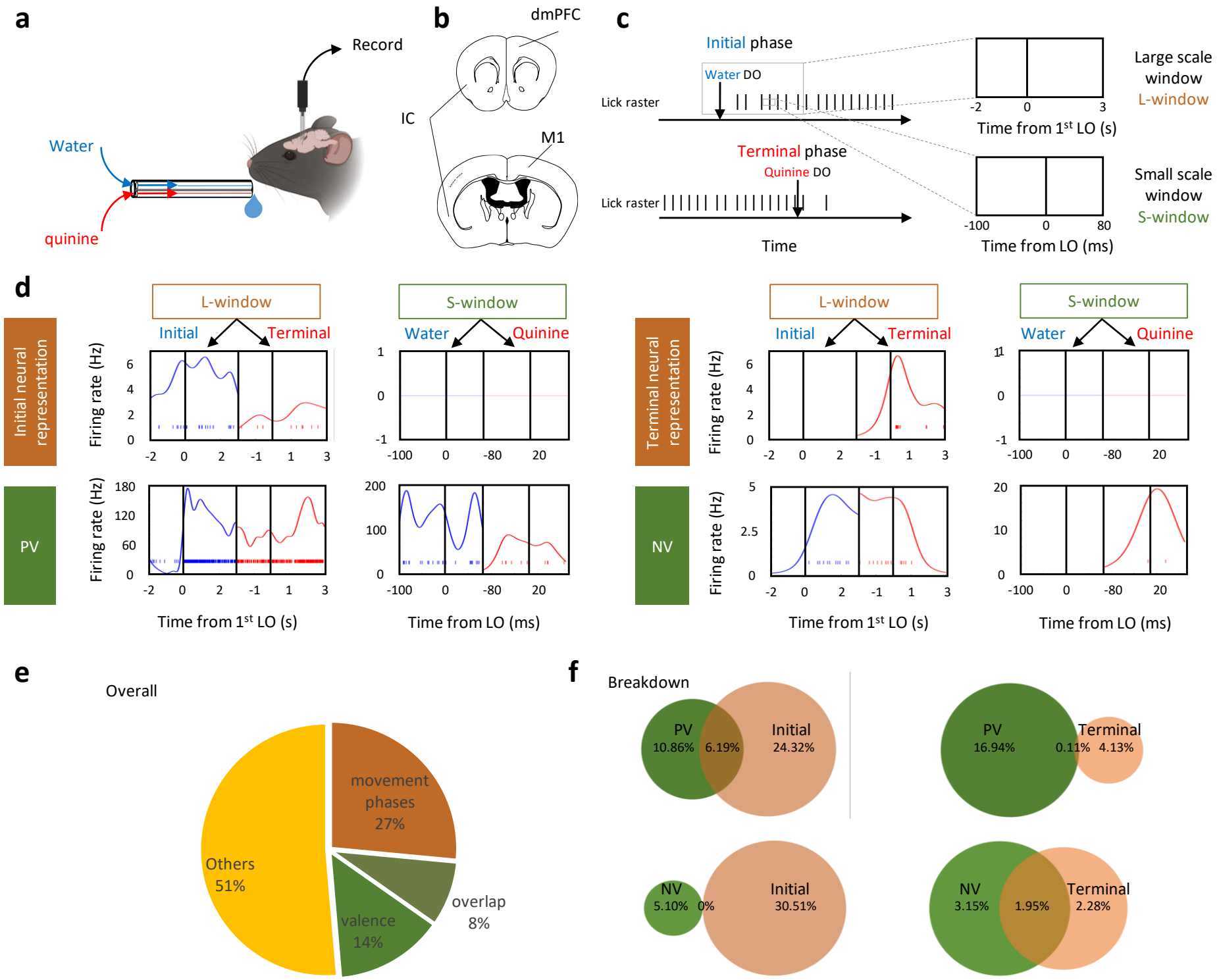
a
Record
Water
quinine
b
dmPFC
IC
M1
c
Initial phase
Water DO
Lick raster
Time from 1st LO (s)
Large scale window
L-window
Terminal phase
Quinine DO
Lick raster
Time
Time from LO (ms)
Small scale window
S-window
d
Initial neural representation
PV
L-window
S-window
Initial
Terminal
Water
Quinine
Firing rate (Hz)
Time from 1st LO (s)
Time from LO (ms)
Terminal neural representation
NV
e
Overall
movement phases 27%
overlap 8%
valence 14%
Others 51%
f
Breakdown
PV 10.86% 6.19% Initial 24.32%
PV 16.94% 0.11% 4.13% Terminal
NV 5.10% 0% Initial 30.51%
NV 3.15% 1.95% Terminal 2.28%

Fig 2

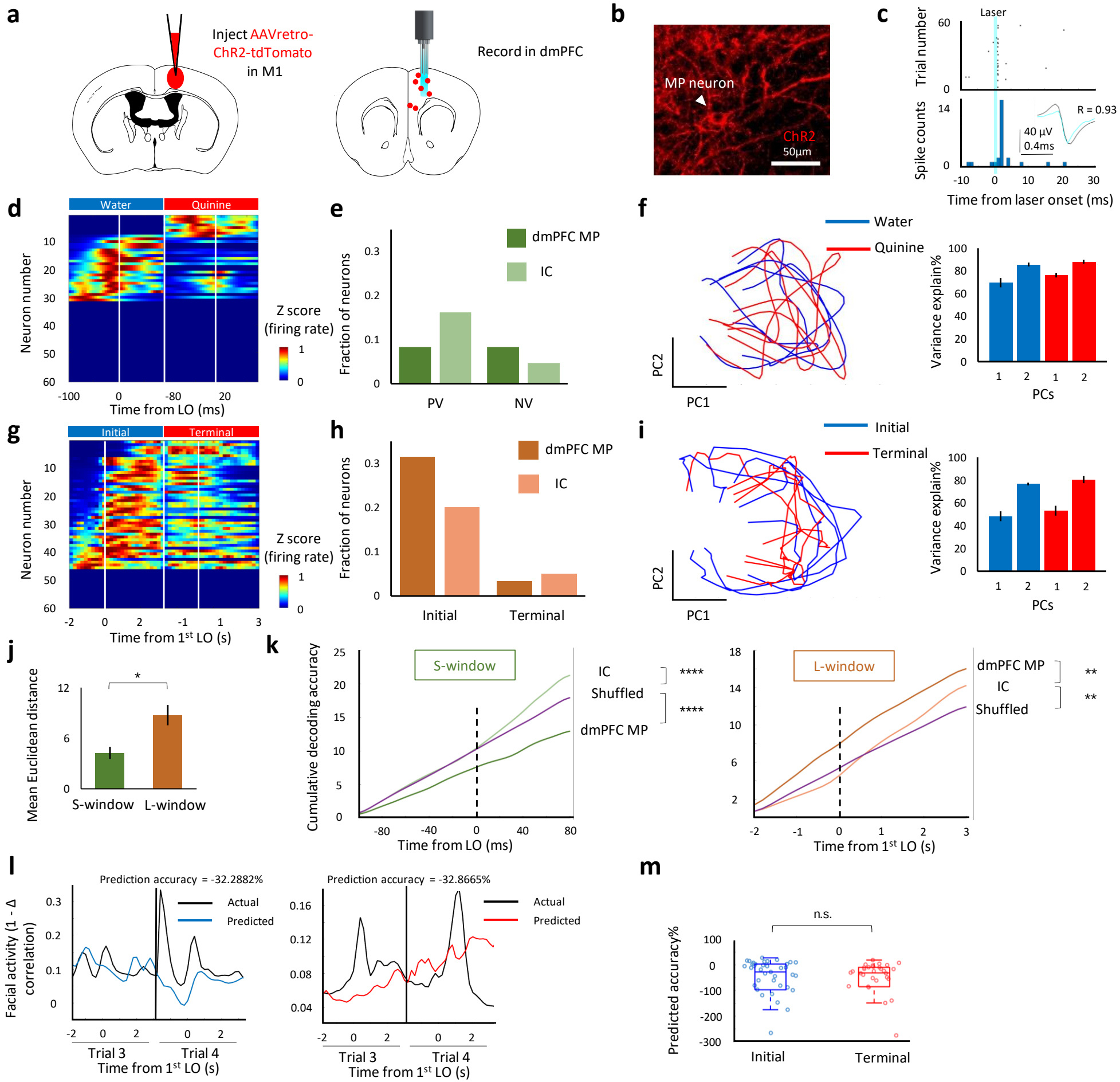
a
Inject AAVretro-ChR2-tdTomato in M1
Record in dmPFC
b
MP neuron
ChR2
50µm
c
Laser
Trial number
Spike counts
R = 0.93
40 µV
0.4ms
Time from laser onset (ms)
d
Water
Quinine
Neuron number
Z score (firing rate)
Time from LO (ms)
e
dmPFC MP
IC
Fraction of neurons
PV
NV
f
Water
Quinine
PC2
PC1
Variance explain%
PCs
g
Initial
Terminal
Neuron number
Z score (firing rate)
Time from 1st LO (s)
h
dmPFC MP
IC
Fraction of neurons
Initial
Terminal
i
Initial
Terminal
PC2
PC1
Variance explain%
PCs
j
Mean Euclidean distance
S-window
L-window
k
S-window
Cumulative decoding accuracy
IC
Shuffled
dmPFC MP
Time from LO (ms)
L-window
dmPFC MP
IC
Shuffled
Time from 1st LO (s)
l
Prediction accuracy = -32.2882%
Actual
Predicted
Facial activity (1 - Δ correlation)
Trial 3
Trial 4
Time from 1st LO (s)
Prediction accuracy = -32.8665%
Actual
Predicted
Trial 3
Trial 4
Time from 1st LO (s)
m
n.s.
Predicted accuracy%
Initial
Terminal

Fig 3

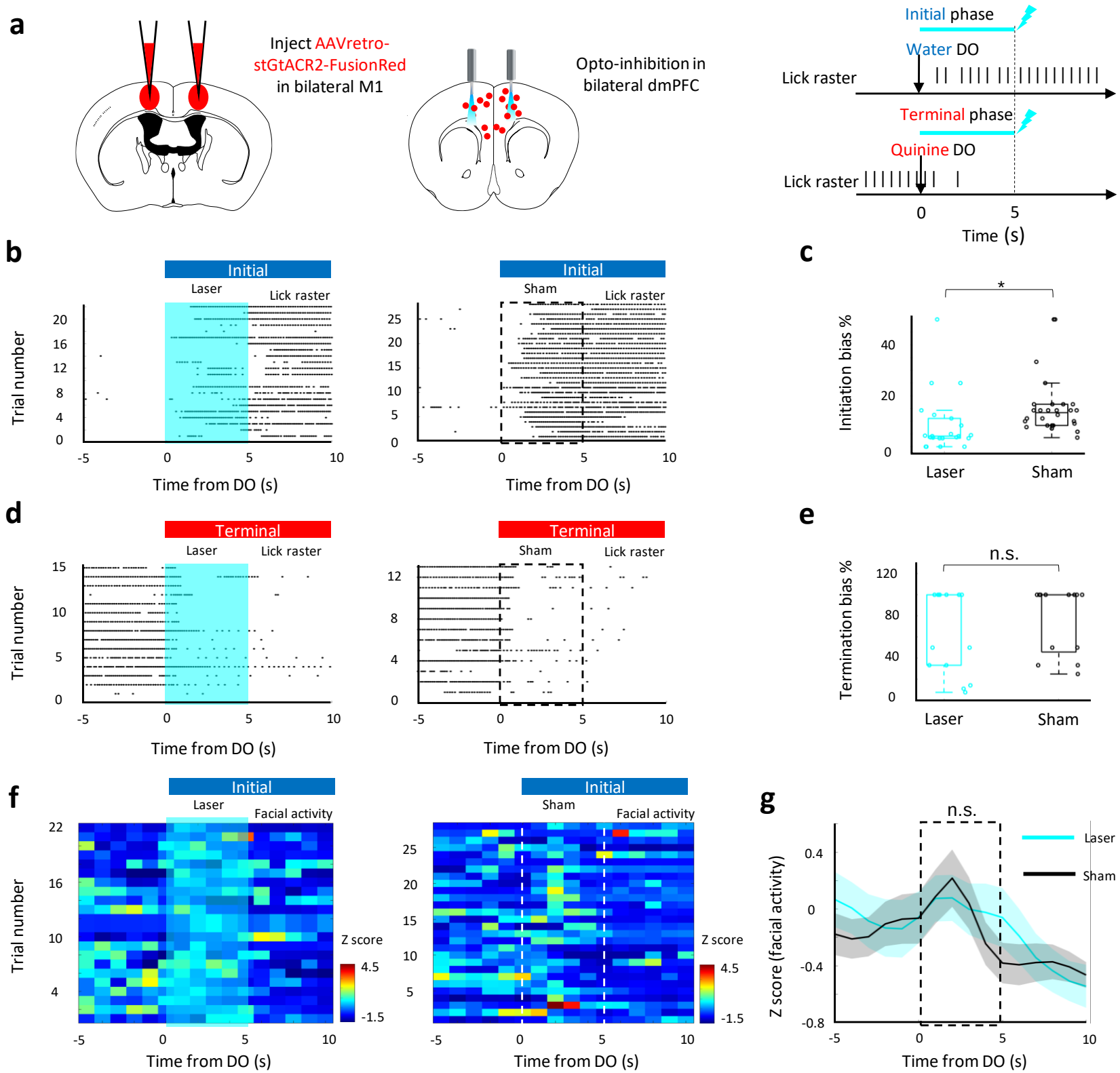
a
Inject AAVretro-stGtACR2-FusionRed in bilateral M1
Opto-inhibition in bilateral dmPFC
Initial phase
Water DO
Lick raster
Terminal phase
Quinine DO
Lick raster
0
5
Time (s)
b
Initial
Laser
Lick raster
Trial number
Time from DO (s)
Initial
Sham
Lick raster
Time from DO (s)
c
*
Initiation bias %
Laser
Sham
d
Terminal
Laser
Lick raster
Trial number
Time from DO (s)
Terminal
Sham
Lick raster
Time from DO (s)
e
n.s.
Termination bias %
Laser
Sham
f
Initial
Laser
Facial activity
Trial number
Z score
4.5
-1.5
Time from DO (s)
Initial
Sham
Facial activity
Z score
4.5
-1.5
Time from DO (s)
g
n.s.
Laser
Sham
Z score (facial activity)
Time from DO (s)

Fig 4

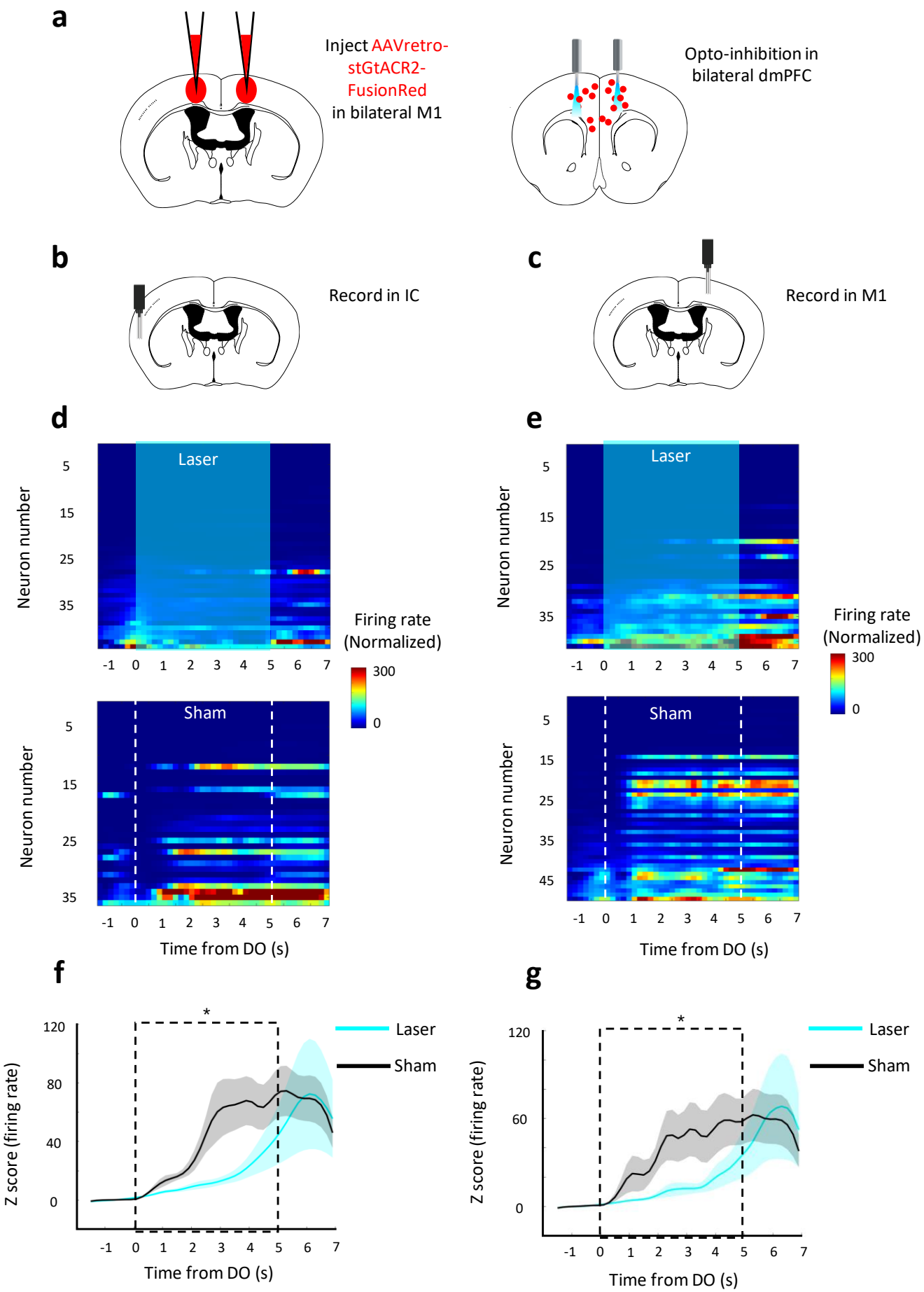
a
Inject AAVretro-stGtACR2-FusionRed in bilateral M1
Opto-inhibition in bilateral dmPFC
b
Record in IC
c
Record in M1
d
Laser
Sham
Neuron number
Time from DO (s)
Firing rate (Normalized)
300
0
e
Laser
Sham
Neuron number
Time from DO (s)
Firing rate (Normalized)
300
0
f
Laser
Sham
Z score (firing rate)
Time from DO (s)
g
Laser
Sham
Z score (firing rate)
Time from DO (s)

Fig 5

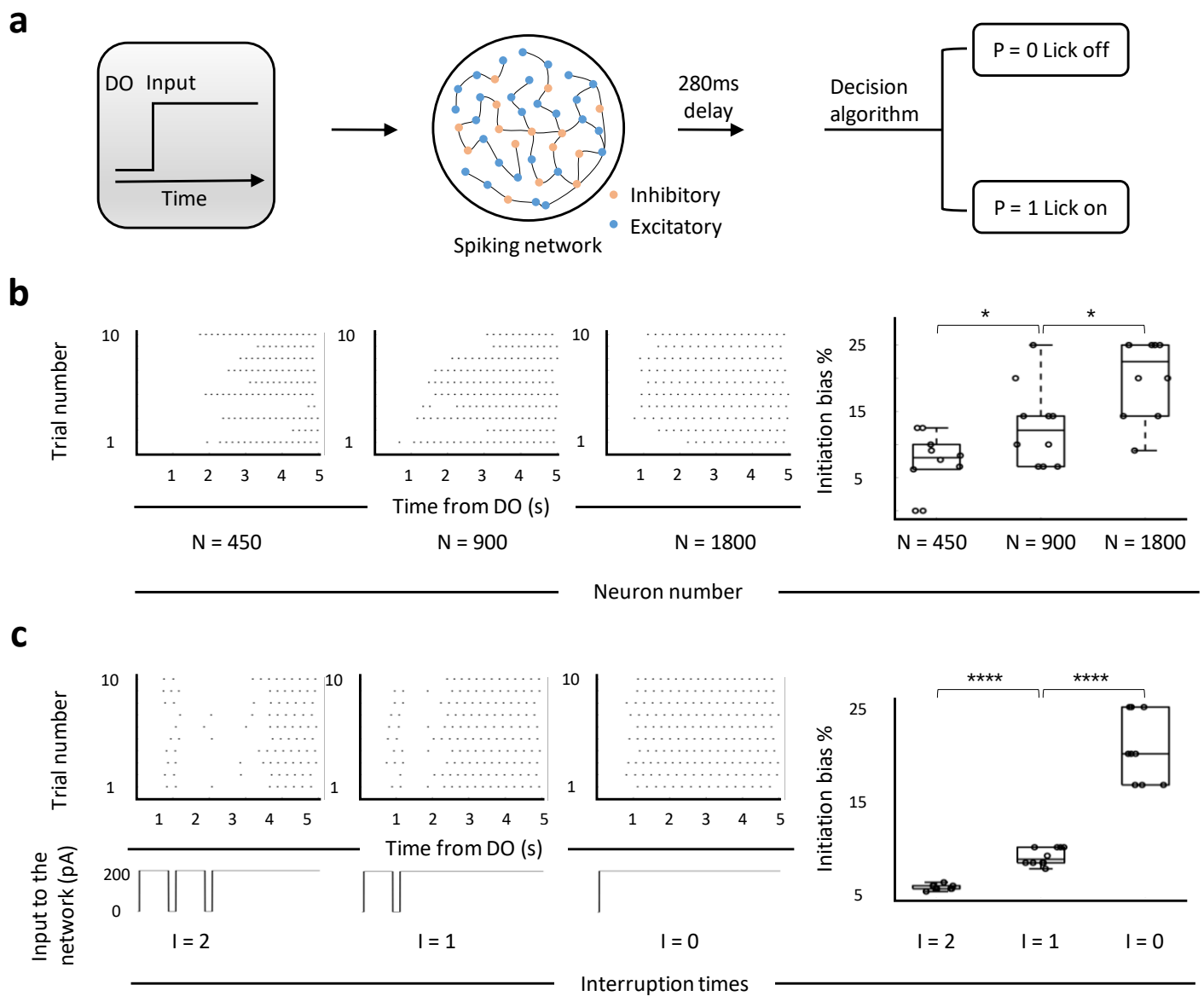
a
DO Input
Time
Spiking network
Inhibitory
Excitatory
280ms delay
Decision algorithm
P = 0 Lick off
P = 1 Lick on
b
Trial number
Time from DO (s)
N = 450
N = 900
N = 1800
Initiation bias %
Neuron number
c
Input to the network (pA)
I = 2
I = 1
I = 0
Interruption times

Fig 6

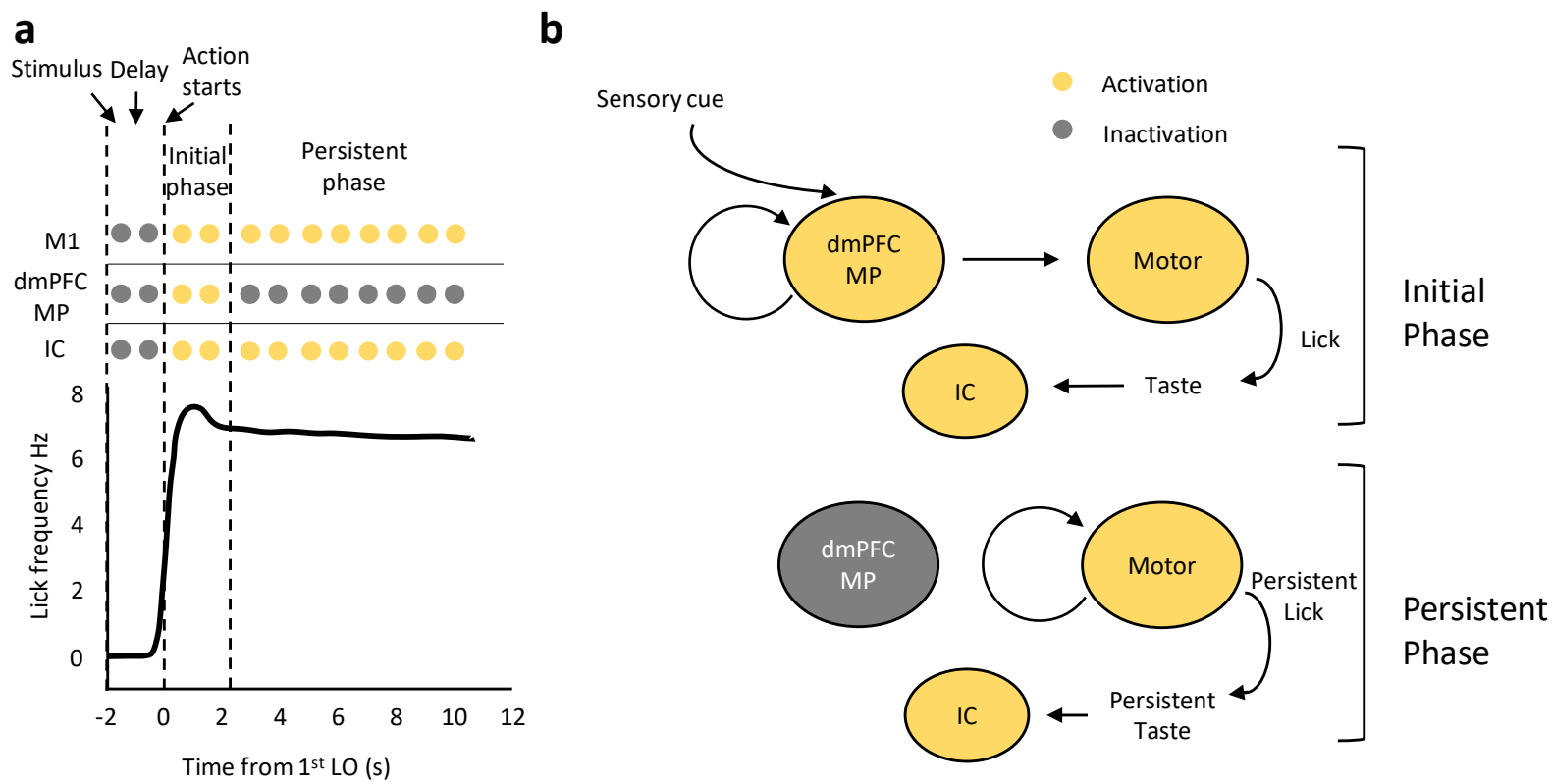
a
Stimulus Delay
Action starts
Initial phase
Persistent phase
M1
dmPFC MP
IC
Lick frequency Hz
8
6
4
2
0
-2
0
2
4
6
8
10
12
Time from 1st LO (s)
b
Sensory cue
Activation
Inactivation
dmPFC MP
Motor
Lick
IC
Taste
Initial Phase
dmPFC MP
Motor
Persistent Lick
IC
Persistent Taste
Persistent Phase

Supplementary Fig 1

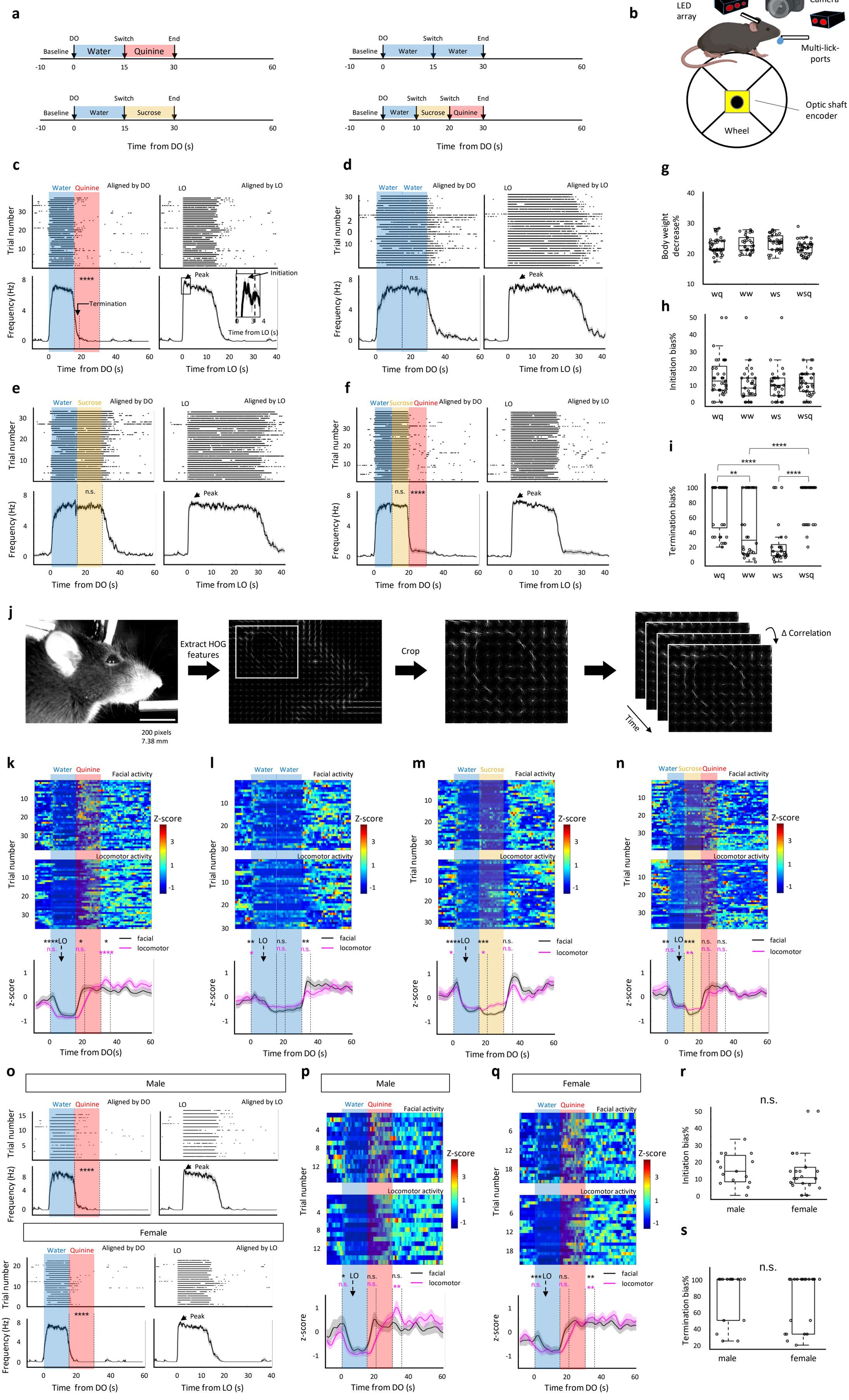

Supplementary Fig 2

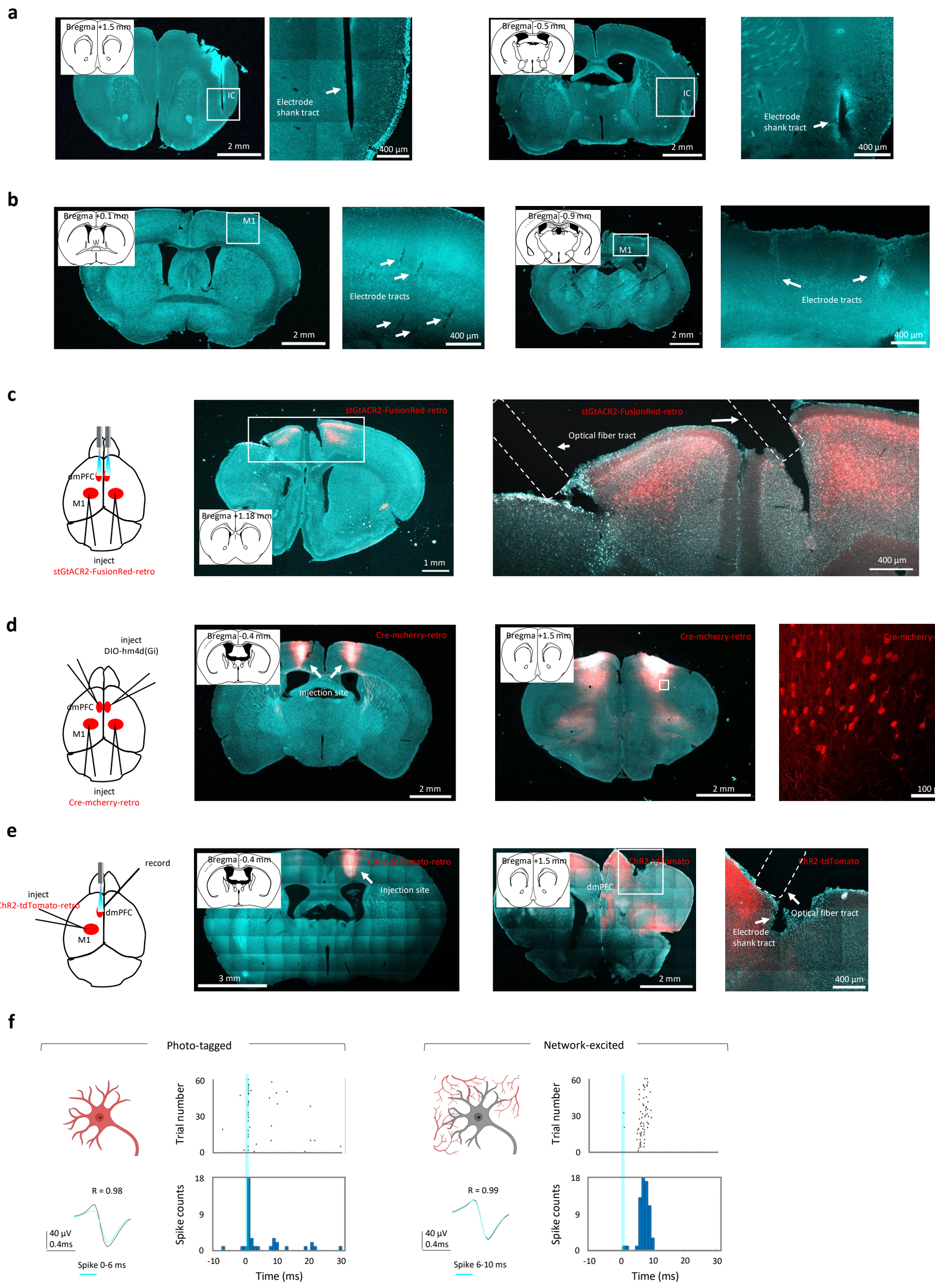

Supplementary Fig 3

Cell classification to discriminate water and quinine-licks

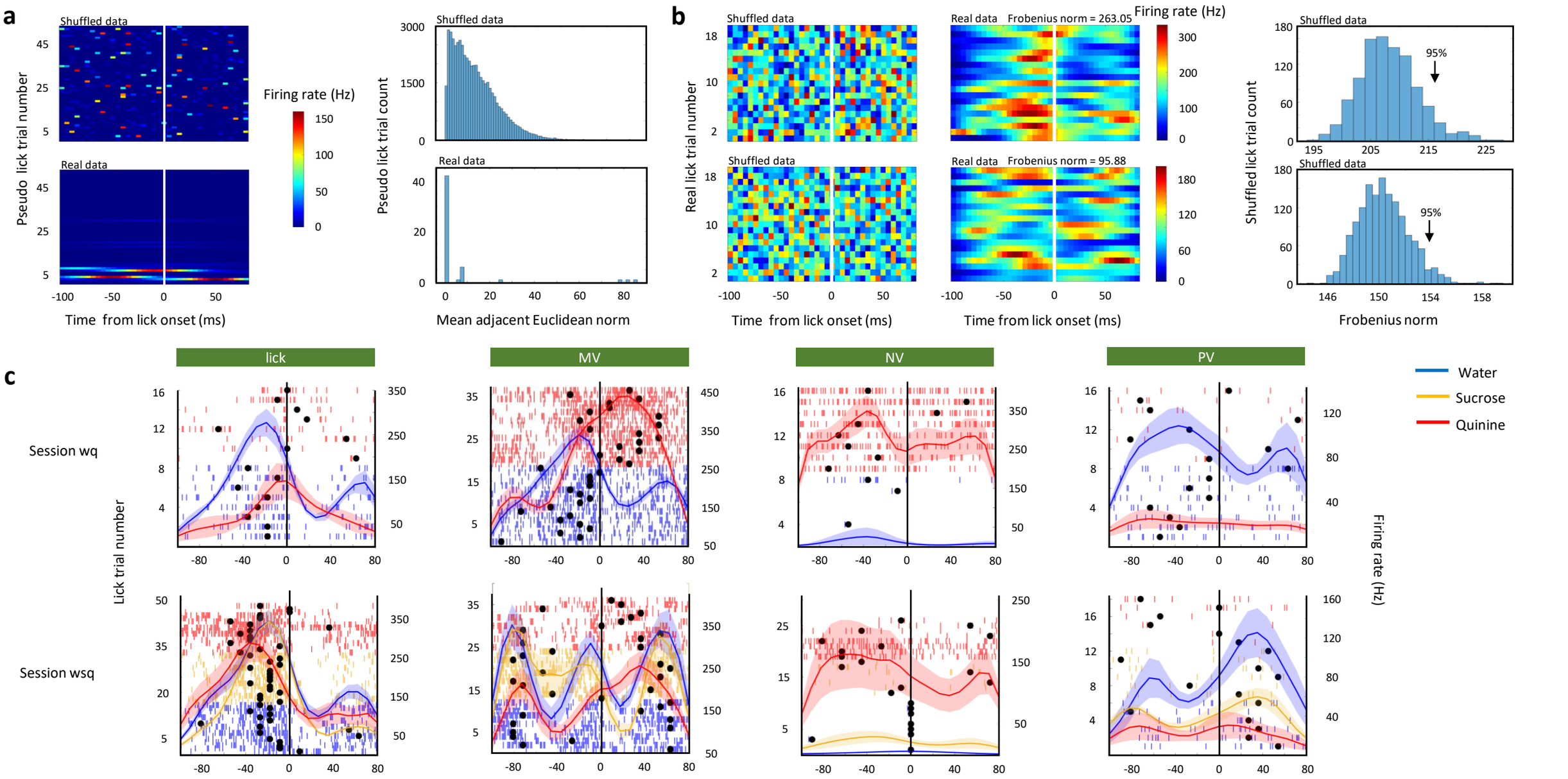

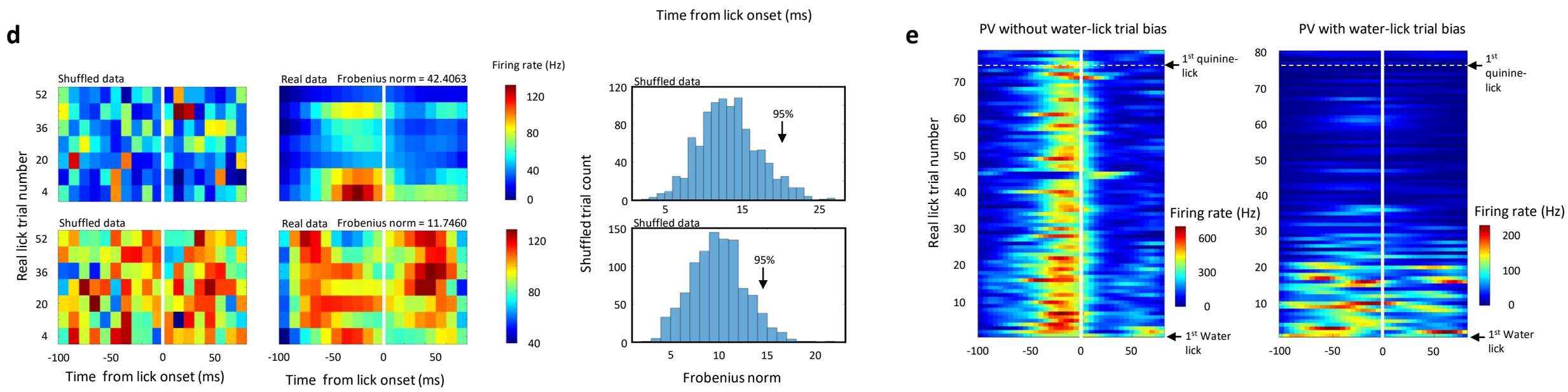

Cell classification to discriminate initial and terminal phase

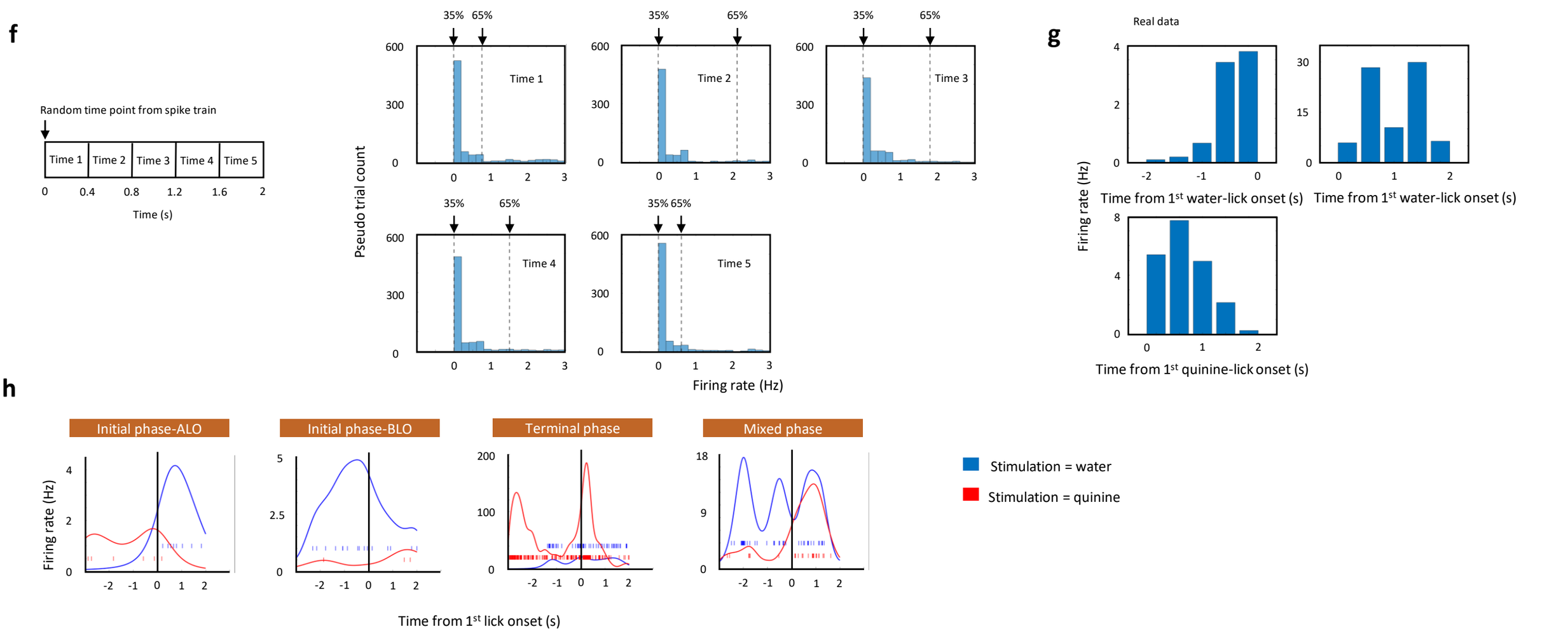

Supplementary Fig 4

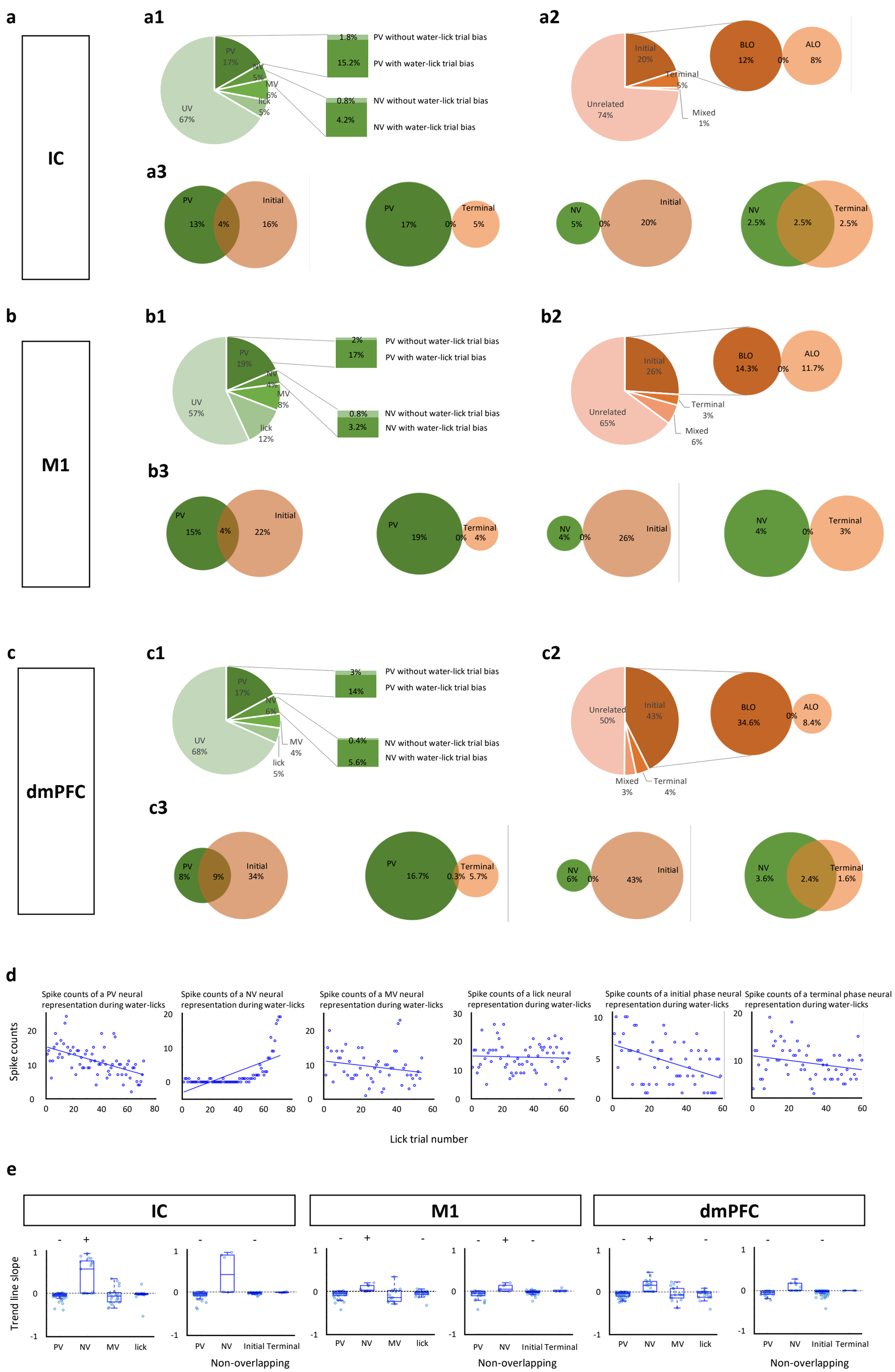

Supplementary Fig 5

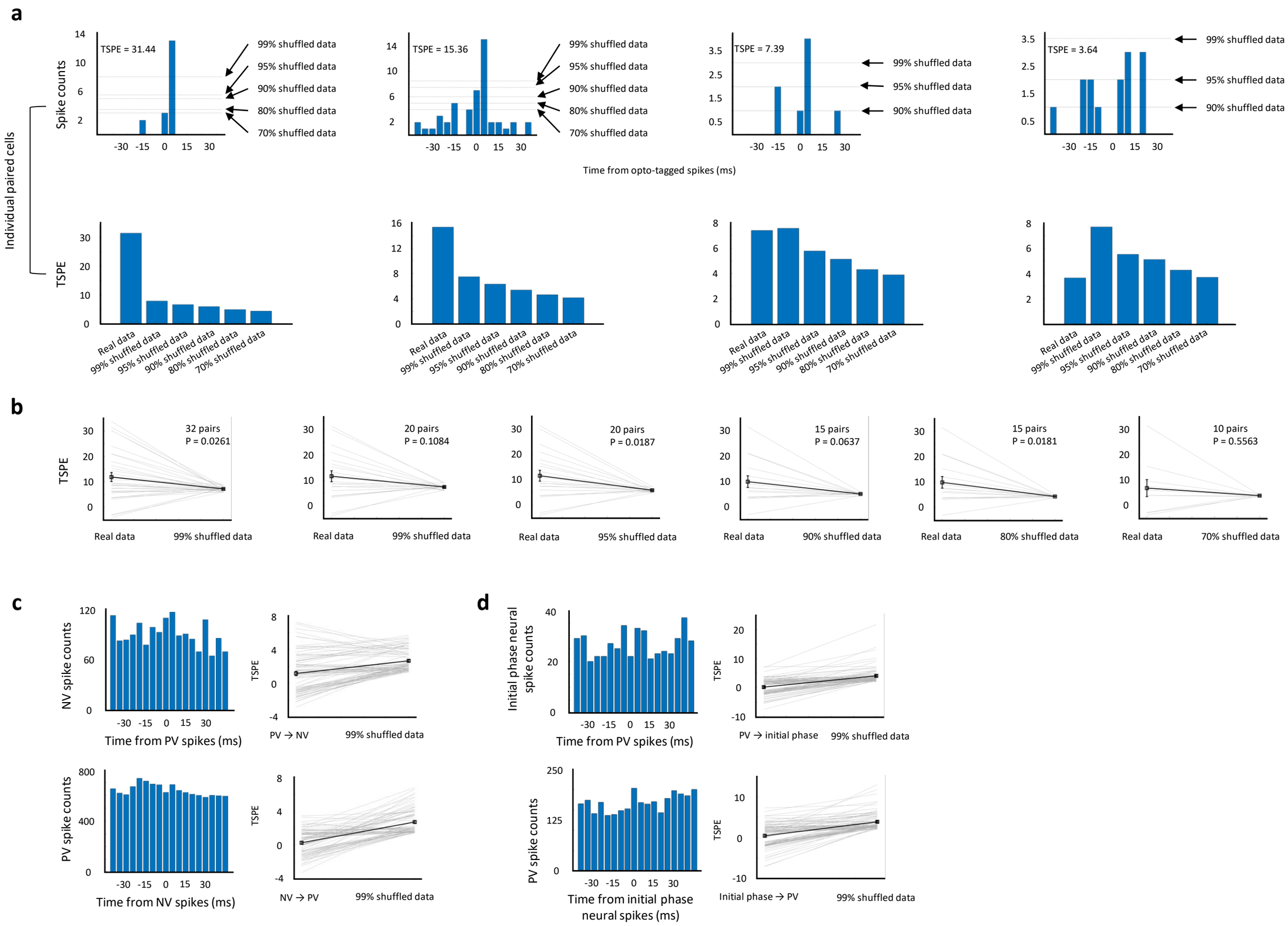

Supplementary Fig 6

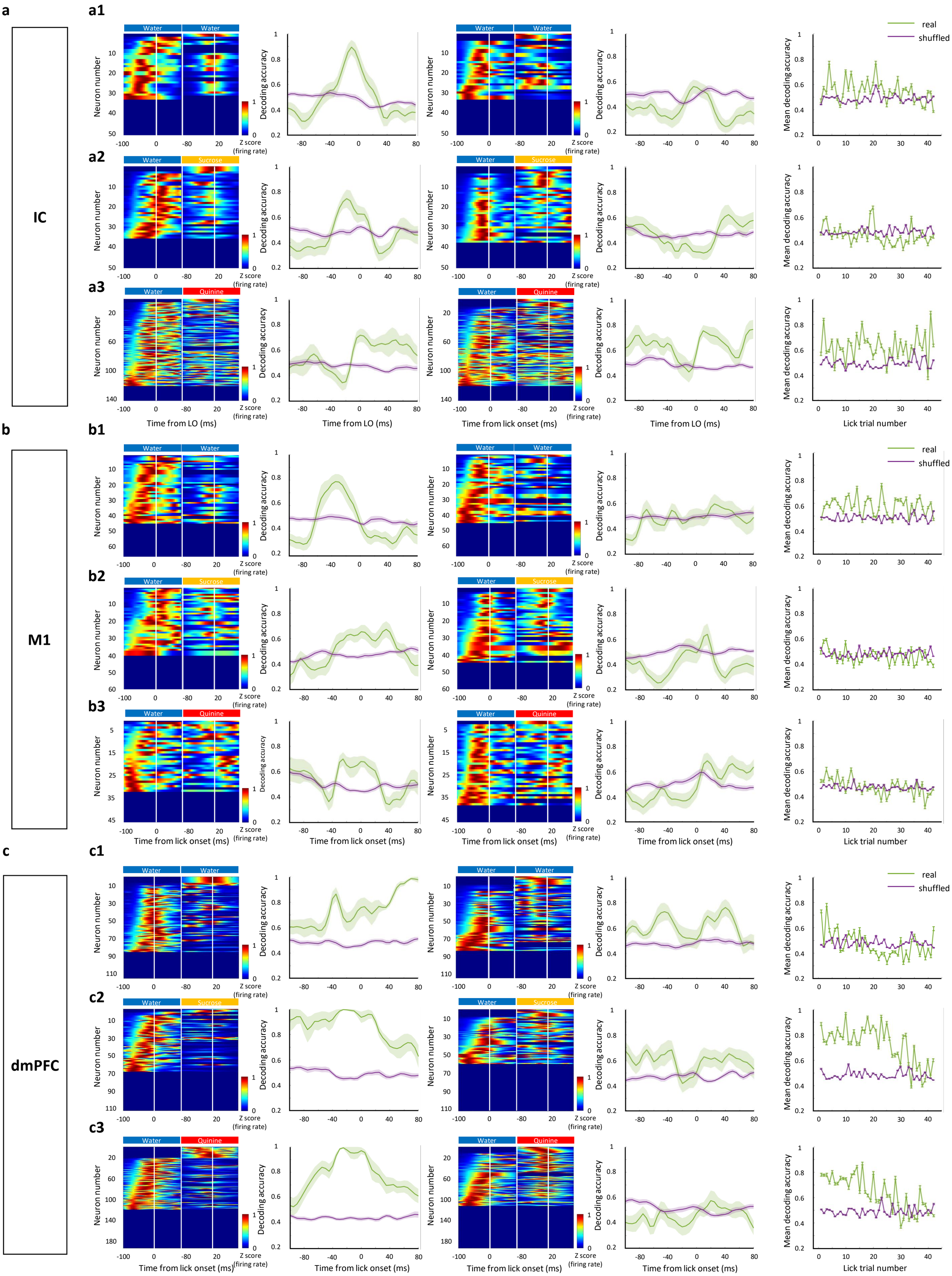

Supplementary Fig 7

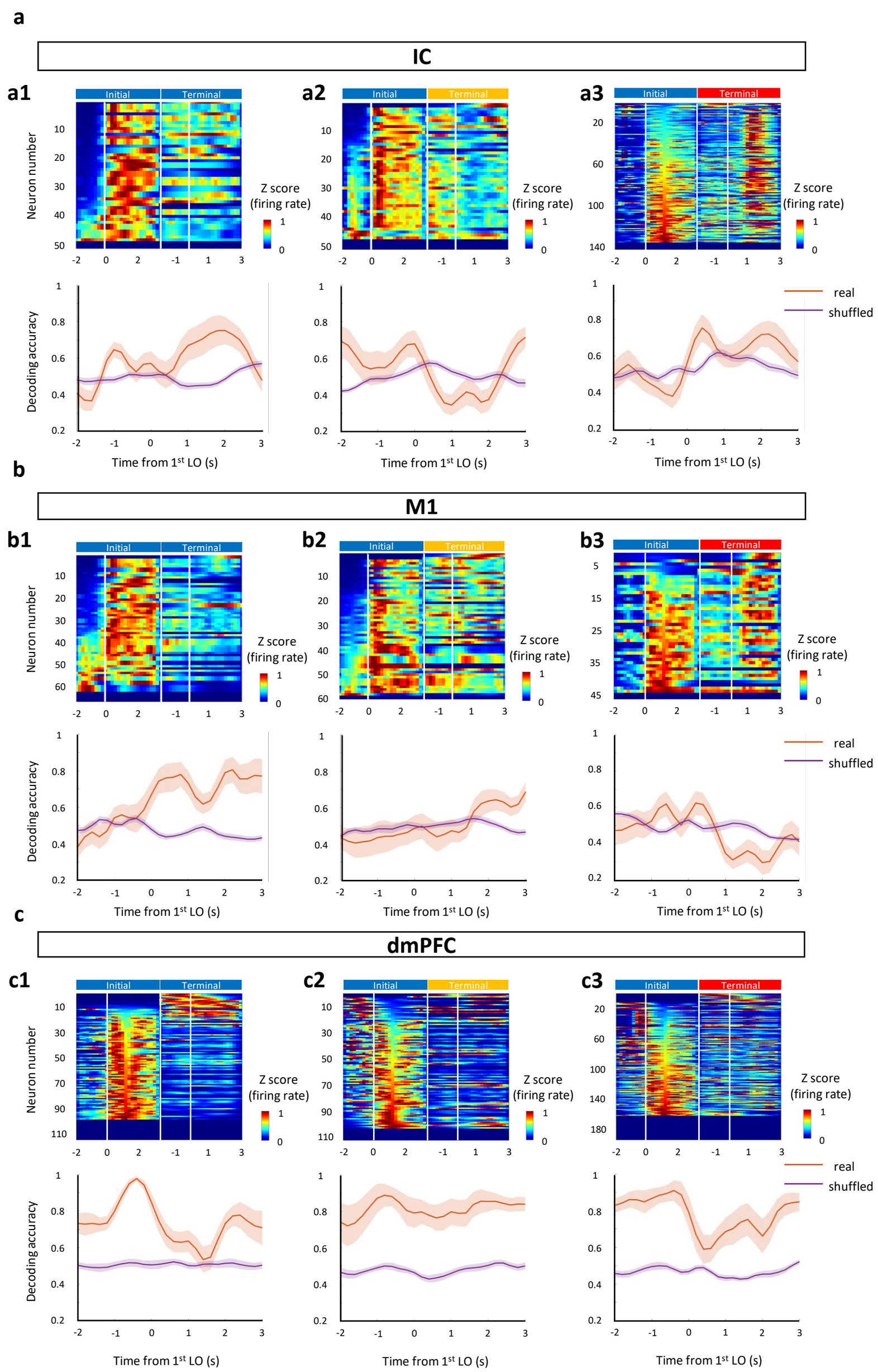

Supplementary Fig 8

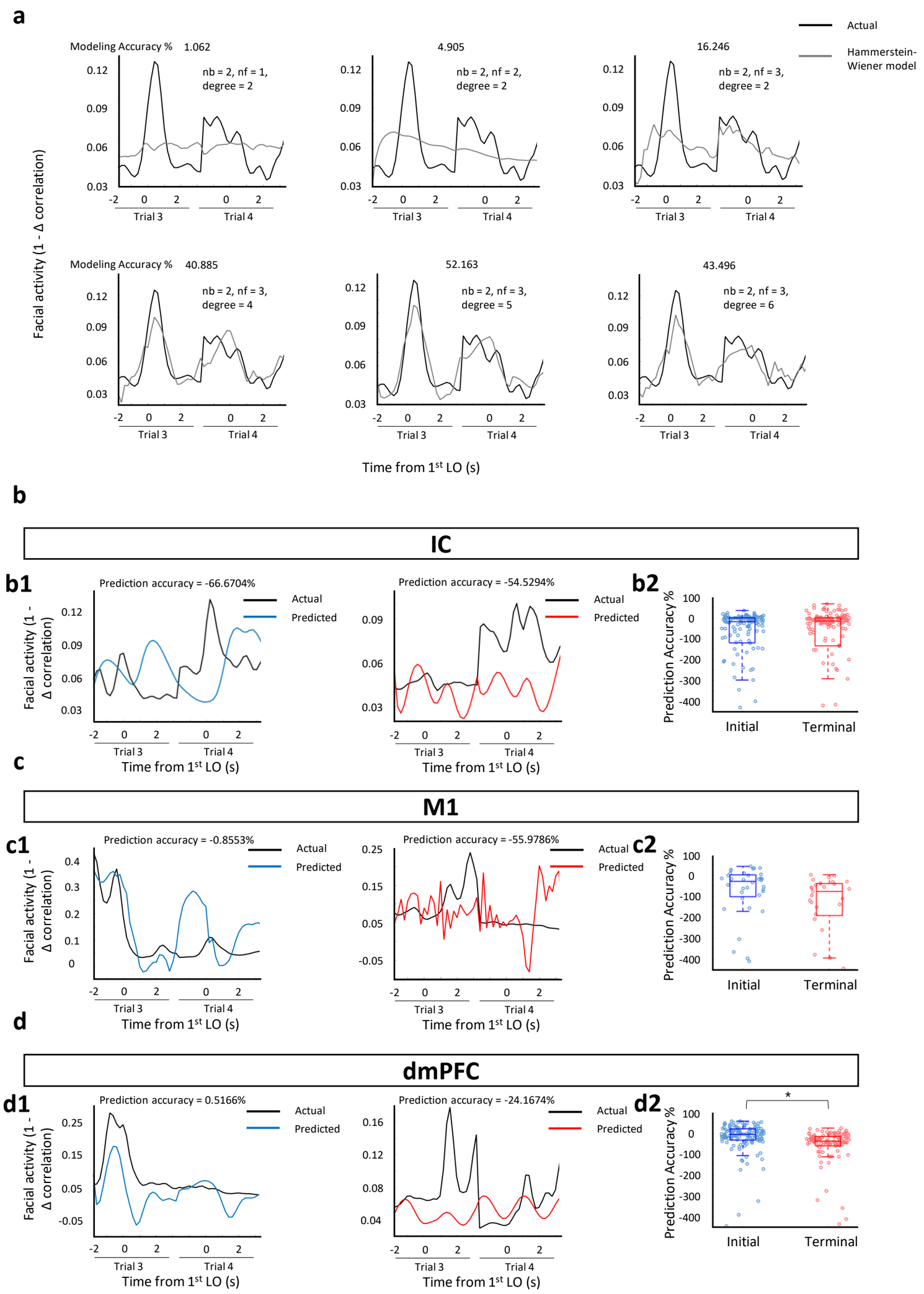

Supplementary Fig 9

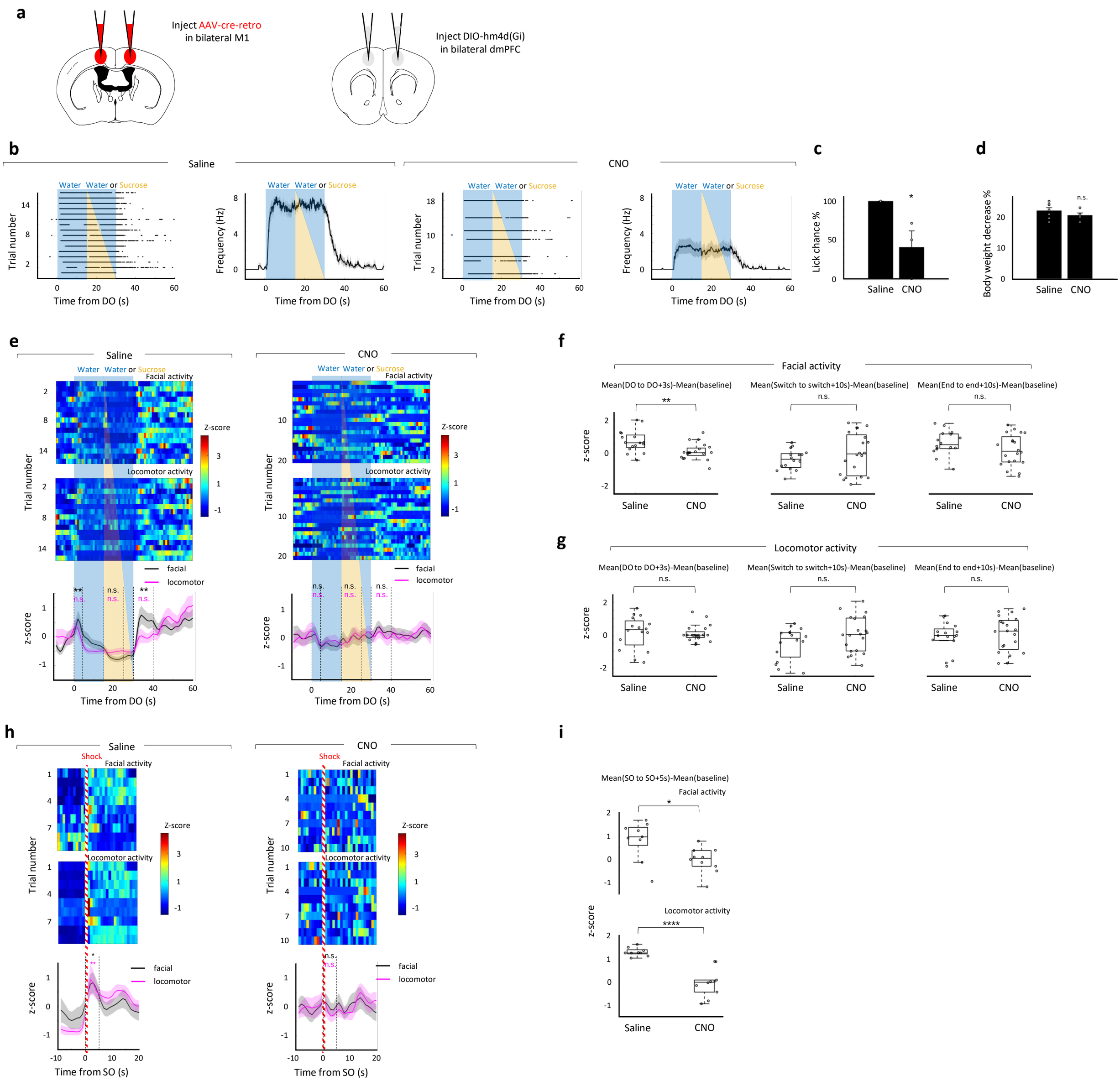

Supplementary Fig 10

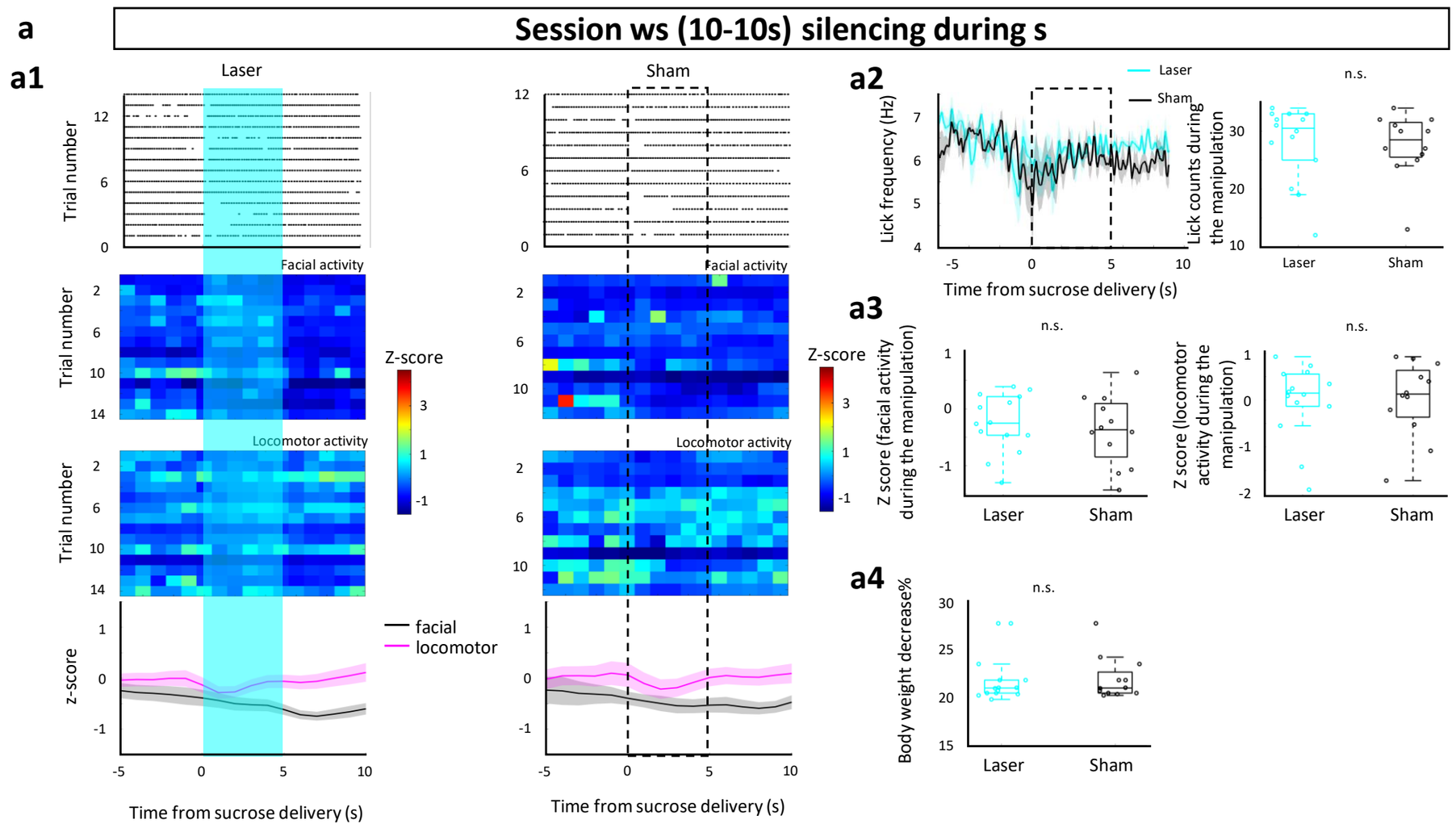

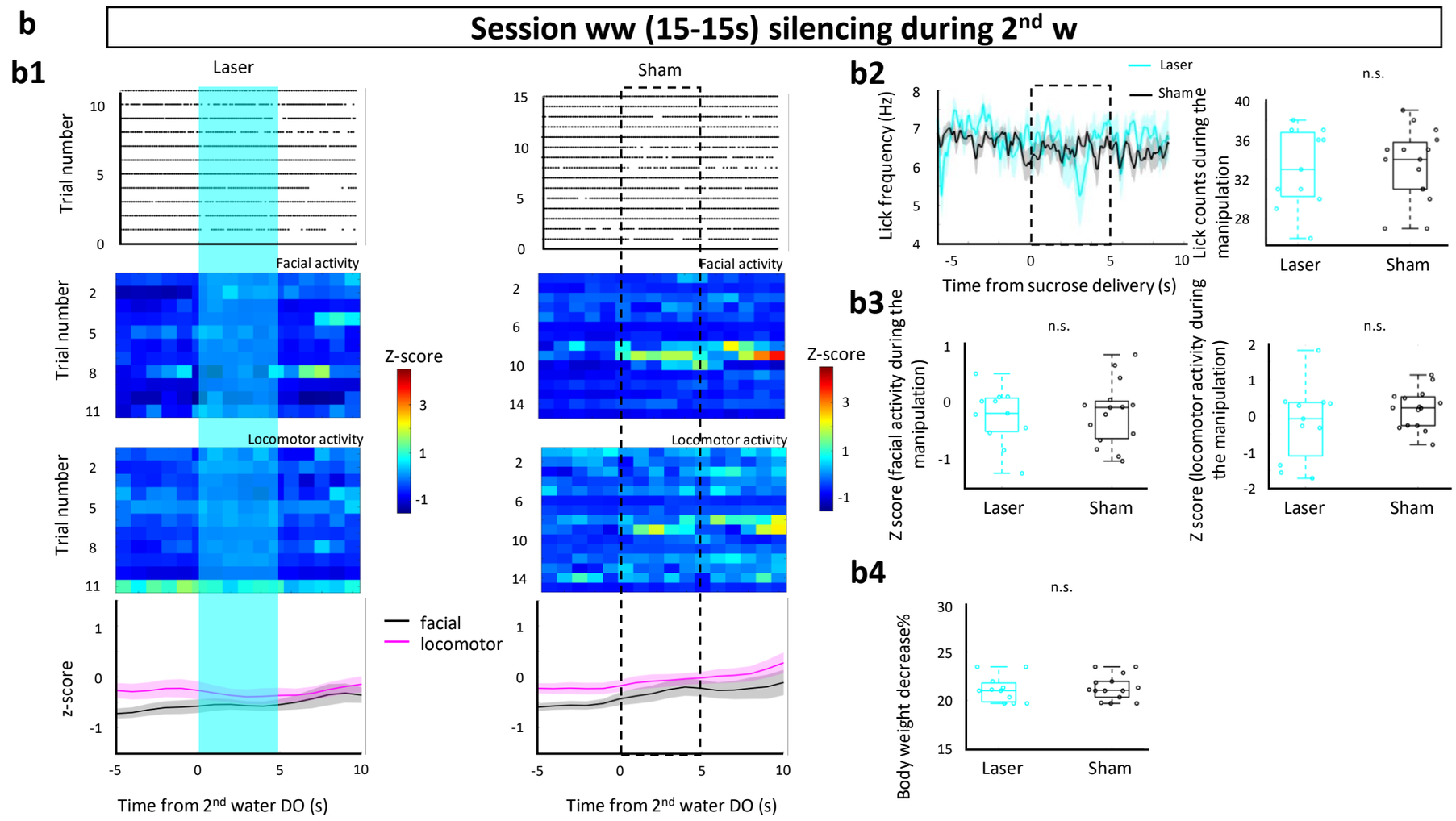

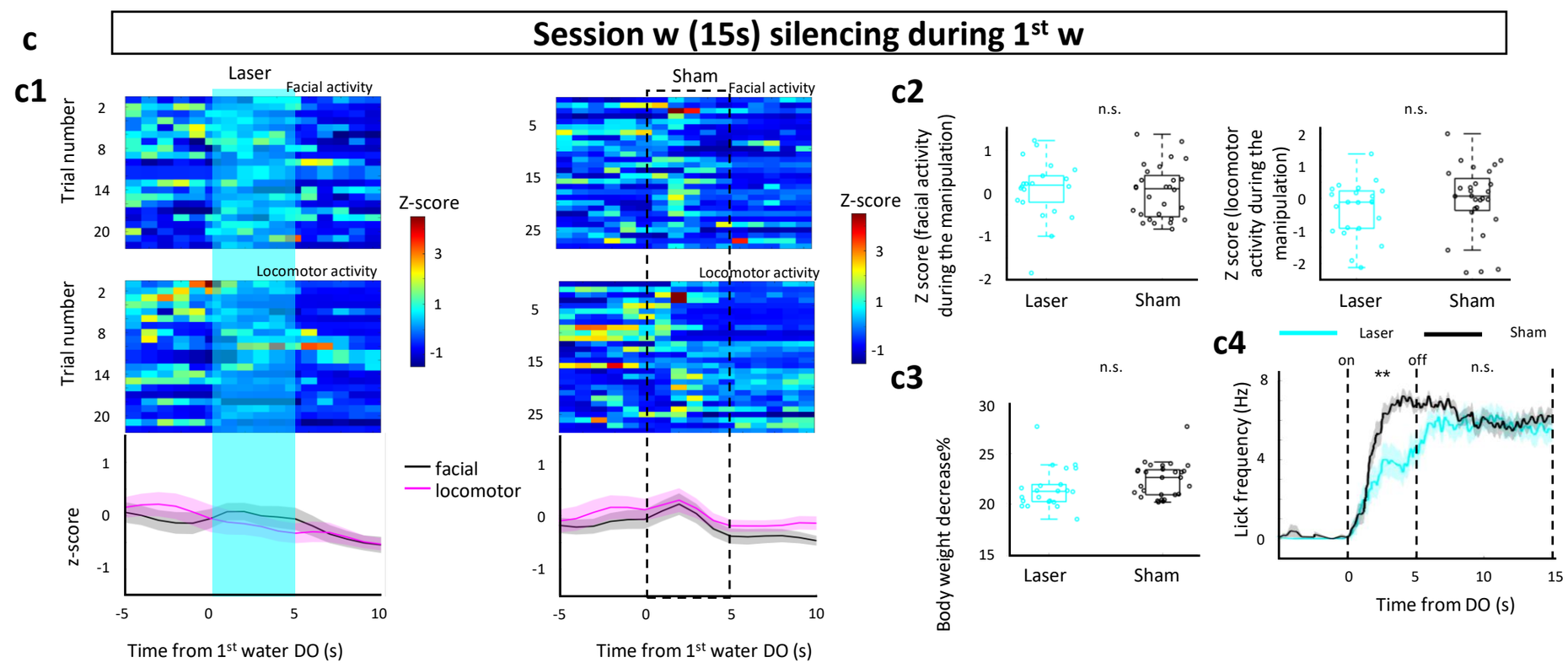

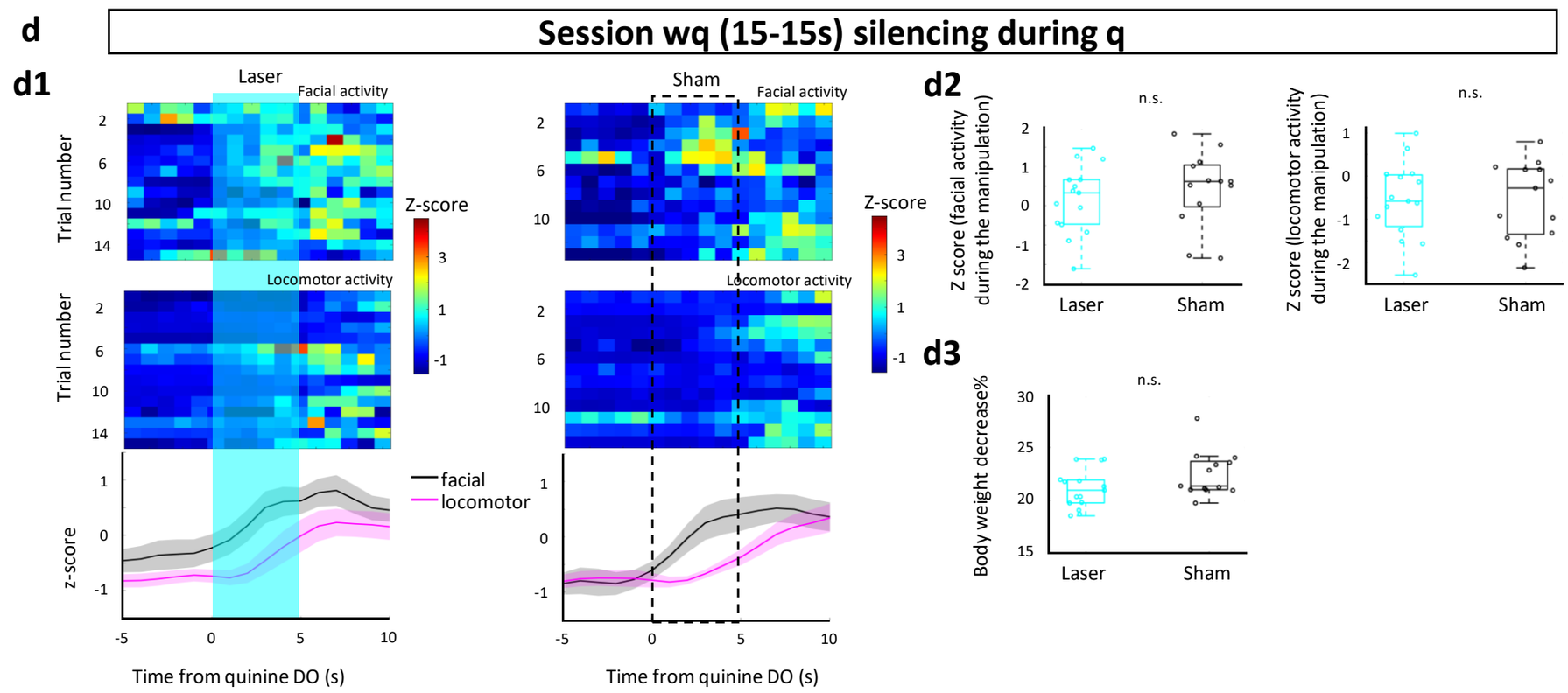
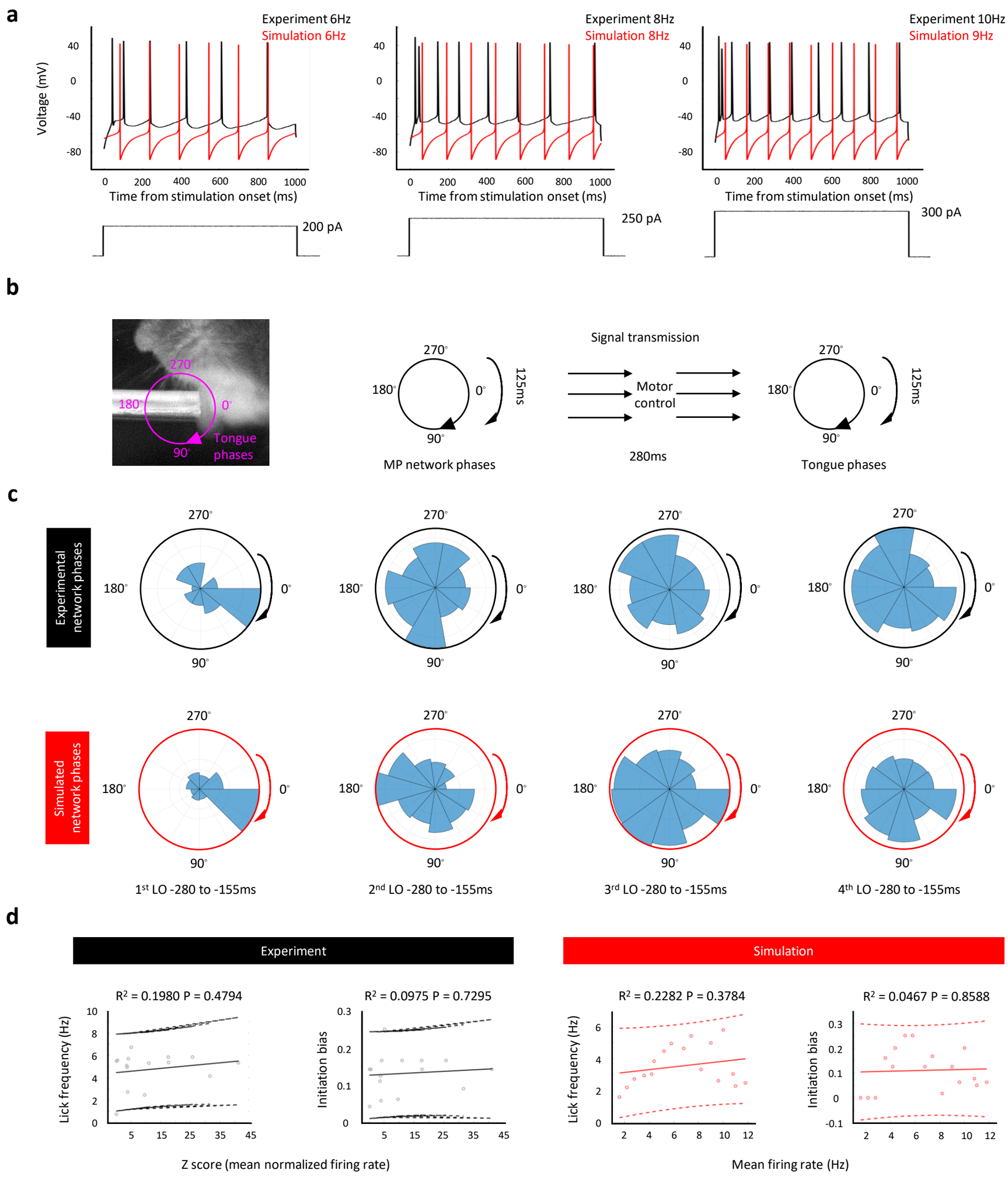
Supplementary Fig 11